Chemically Accurate ab Initio Potential Energy Surfaces for the Lowest $^3A'$ and $^3A''$ Electronically Adiabatic States of O(^{3}P) + H_2[†]

Stephanie Rogers,[‡] Desheng Wang, and Aron Kuppermann*

Arthur Amos Noyes Laboratory of Chemical Physics, Division of Chemistry and Chemical Engineering, California Institute of Technology, Pasadena, California 91125

Stephen Walch

Thermosciences Institute, NASA Ames Research Center, MS 230-3, Moffett Field, California 94035-1000

Received: August 23, 1999; In Final Form: November 17, 1999

The electronic energies of the lowest $^3A'$ and $^3A''$ states of the O(^{3}P) + H_2 system were calculated for 951 geometries using MOLPRO. The calculations were fitted by a rotating Morse spline method and independently by a generalized London−Eyring−Polanyi−Sato (LEPS) double-polynomial method. A higher accuracy calculation for 112 of these geometries was also performed for both $^3A'$ and $^3A''$ to obtain correction potential energy surfaces (PESs) used to raise the accuracy of the original surfaces to about 0.3 kcal/mol. The resulting fitted PESs are presented and compared to each other and to a previous empirical LEPS surface.

1. Introduction

The reaction of O(^{3}P) with H_2 is of fundamental interest to chemical dynamics. It is known to be a major participant in combustion processes[1] and is also of importance in atmospheric reactions as the OH radical produced is a reactive species in ozone chemistry.[2] Experimental thermal and some state-resolved rate constants for this reaction have been obtained over a wide range of temperatures.[1,3−5] Its reaction dynamics are, however, difficult to study experimentally. The cross sections for the O(^{1}D) + H_2 reaction at low energies (∼0.5 eV) are larger than those of the O(^{3}P)+ H_2 one by about 6 orders of magnitude or more.[6,7] As a result, any source of O(^{3}P) atoms having a small amount (∼1 ppm) of O(^{1}D) atoms will make O(^{3}P) reactions undetectable at these energies. Theoretical studies are therefore strongly indicated. The cumulative reaction probability for zero total angular momentum *J* has previously been obtained by an accurate 3D reactive scattering calculation.[8] Several approximate methods for calculating reaction probabilities and rate constants have also been used, including quasiclassical trajectory (QCT),[9−13] transition-state theory (TST),[14−20] and collinear exact quantum (CEQ) approaches.[11,21−24] All of these studies have used potential energy surfaces (PESs) of less than chemical accuracy,[2,6,9,10,12,14,15,17−28] but nevertheless give rate constants in reasonable agreement with experiment. However, in terms of state-to-state dynamics those PESs are not sufficiently accurate. A series of papers comparing the reaction dynamics on several available potential energy surfaces revealed disagreement among the surfaces and among different reactive scattering methods.[13,18,21,29−31] This, along with the current inability to study the state-resolved reaction dynamics experimentally, suggests the need for a potential energy surface of chemical accuracy.

Recent developments in electronic structure theory make it possible to obtain PESs of chemical accuracy for this system. These include the internally contracted configuration interaction (ICCI) method,[32,33] which can be used to routinely carry out CI calculations equivalent to diagonalizing a matrix of order several million, and utilization of correlation-consistent basis sets of different sizes, which can be used to extrapolate to the basis set limit.[34] These methods should permit calculations for the O + H_2 system that are accurate to a few tenths of a kcal/mol.

Several mathematical forms exist that give reasonably accurate fits to ab initio data. The rotating Morse spline (RMOS) form is known to give good results.[35−43] Bowman et al. have used this method to fit ab initio data for the HOCl system to within 0.05 kcal/mol average absolute value error.[44] Other methods have been developed recently that promise accurate fitting, appropriate physical behavior, and smooth derivatives. Rabitz and co-workers developed the reproducing kernel Hilbert-space method and achieved good results for the O(^{1}D) + H_2 system.[45,46] Jordan et al. have used an interpolation scheme to fit the OH + H_2[47] PES, and Kouri and co-workers have used the distributed approximating functional (DAF) method to fit H_3 ab initio data with good results.[48] Another method that has been used with various mathematical variants is a many-body expansion approach.[49−53] With the recent development of more accurate fitting forms, and accurate ab initio data, a potential energy surface of chemical accuracy for the O(^{3}P) + H_2 system is realizable.

The objective of achieving a quantitatively correct description of the dynamics of this system with the help of accurate quantum reactive scattering calculations would be jeopardized if a potential energy surface of inadequate accuracy were to be used. Such scattering calculations are computationally intensive, requiring the use of massively parallel computers with ample memory and storage space.[54−56] To perform such calculations on a potential energy surface that is not sufficiently accurate would, in addition, be an inappropriate utilization of such resources.

In this paper we present a chemically accurate (within about 0.3 kcal/mol) representation of the O(^{3}P) + H_2 lowest $^3A'$ and $^3A''$ PESs. In section 2 the methods used are described. We compare the PESs obtained in section 3 and give a summary in section 4.

[†] Work supported in part by NSF Grant CHE-9810050. S.P.W. was supported by NASA Contract NAS2-14031 to ELORET.

* To whom correspondence should be addressed. Email: aron@caltech.edu.

[‡] Work done in partial fulfillment of requirements for Ph.D. in Chemistry.

10.1021/jp992985g CCC: $19.00

2. Methods

2.1. Electronic Energy. We have performed complete-active-space-self-consistent-field (CASSCF) ICCI calculations using correlation-consistent basis sets.[34] Two basis sets were used. The calculations denoted in this paper by "regular accuracy" use the correlation-consistent polarized valence quadruple-ζ (cc-pVQZ) basis set[34] plus one set of even-tempered spd functions on O[57] and the cc-pVQZ basis set minus the f functions plus one set of even-tempered sp functions on H.[57] The calculations denoted by "high accuracy" use the correlation-consistent polarized valence quintuple ζ (cc-pV5Z) basis set on O and H plus the same set of even-tempered functions.[57] Some calculations were performed with a correlation-consistent polarized valence triple-ζ (cc-pVTZ) basis set[34] for the purposes of a basis-set extrapolation.

The CASSCF active space is constructed from the O2p-like orbitals and the two orbitals of the HH bond pair. The O1s- and O2s-like orbitals are inactive. For the O(^{3}P) state we use two singly occupied and one doubly occupied O2p orbitals (in a localized orbital description). Tight-diffuse correlation is included by adding an additional O2p′ orbital to the active space to correlate the doubly occupied O2p orbital. This gives an active space of seven a′ and one a″ orbitals for the $^3A''$ state and six a′ and two a″ orbitals for the $^3A'$ state. The ICCI calculations include all configurations generated as single and double excitations from the CASSCF wave function. The O1s-like orbital was frozen in these calculations. Some calculations include the Davidson correction[58] and are denoted ICCI+Q.

2.2. Fitting Methods. Any potential energy surface fitting method should satisfy three criteria. The fitting procedure should be simple, the resulting fitted surface should be in good agreement with the ab initio data, and the mathematical form of the fitting method should be physically realistic in order to minimize the number of ab initio geometries needed to obtain a surface with the correct features and topology.[45,48] We have chosen two different fitting methods, the RMOS and the generalized London−Eyring−Polanyi−Sato double-polynomial (GLDP) methods. Both have been shown to satisfy most of these criteria[38,50] with several successful applications.[35,37−43,49,51−53] Each has been modified to give better results and overcome some of the difficulties encountered in the fitting process.

Regular-accuracy calculations were performed for 951 geometries and high-accuracy ones for a subset of 112 of these geometries. The latter were used to create a correction surface that was applied to the regular-accuracy ab initio data for all 951 geometries to generate high-accuracy data for all of them. This corrected data was then fitted using the RMOS and GLDP methods to give the high-accuracy surfaces. The fitted regular-accuracy surfaces were created by subtracting the correction surface from the fitted high-accuracy surfaces. We will describe the RMOS and the GLDP fitting method, and then the method for fitting the correction surface.

2.2.1. The RMOS Method. The strengths of the RMOS fitting method are its simple, physically realistic mathematical form, and its ability to easily reproduce physical features with a relatively small number of ab initio data without introducing unphysical features.[36,41,43,59−62] The five-parameter Morse function[35,43] is quite flexible, which results in a more accurate fit to the ab initio data than the three-parameter Morse function.

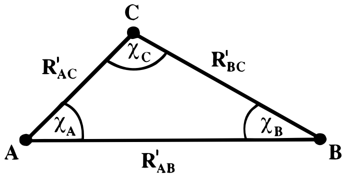

Figure 1. Triatomic system. Bond distances and bond angles in a general triatomic system.

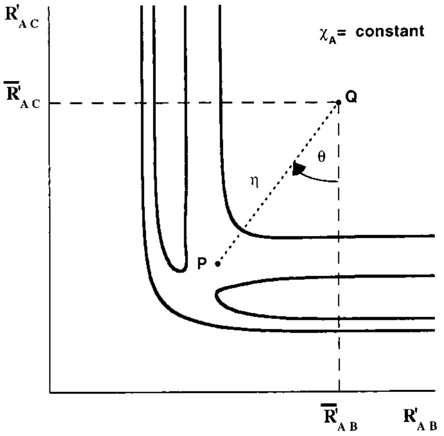

Figure 2. RMOS coordinates. The RMOS coordinates for a point P are η and θ. The curves depict generic equipotential contour lines in the R'_{AB}, R'_{AC} Cartesian coordinate plane, for a fixed bond angle χ_A. Point $Q(\bar{R}'_{AB}, \bar{R}'_{AC})$ is placed on the dissociation plateau.

In a general triatomic system, let ABC denote the three nuclei, R'_{AB}, R'_{BC}, and R'_{AC} the three internuclear distances, and χ_A, χ_B, and χ_C the three bond angles, as depicted in Figure 1. (The primes are used to indicate that these distances are not mass-scaled.) The coordinates used in the RMOS fitting procedure are defined in Figure 2. For a constant χ_A, we select a "swing" point $Q(\bar{R}'_{AB}, \bar{R}'_{AC})$ on the dissociation plateau of the R'_{AB}, R'_{AC} Cartesian coordinate plane. The polar coordinates of a general point $P(R'_{AB}, R'_{AC})$ on this plane with respect to Q are the distance η between P and Q and the "swing" angle θ between the downward vertical line through Q and the QP half-line, in the $0-\pi/2$ range. The values of $\bar{R}'_{AB}$ and $\bar{R}'_{AC}$ are chosen so that for $R'_{AB} > \bar{R}'_{AB}$ (or $R'_{AC} > \bar{R}'_{AC}$) the potential energy function $V(R'_{AB}, R'_{AC}, \chi_A)$ is almost independent of R'_{AB} (or R'_{AC}). In addition, $V(\bar{R}'_{AB}, \bar{R}'_{AC}, \chi_A)$ should be sufficiently large for the scattering wave function obtained using the corresponding fitted PES to be negligible at Q. Within these constraints, it is desirable to make $\bar{R}'_{AB}$ and $\bar{R}'_{AC}$ be as small as possible, so that the PES is not too steep a function of θ in the vicinity of the strong interaction region.

The RMOS fitting form is that of a generalized (five-parameter) Morse function in the variable η, combined with a cubic spline fitting[63] form for the swing and bond angles. The generalized Morse function used is

$$V = D_e[(1 - e^{\beta x})^2 - 1] + V_0 \tag{1}$$

where V_0 specifies the origin of energy

$$\beta = \beta_e(1 + \lambda_1 x + \lambda_2 x^2) \tag{2}$$

and

$$x = \eta - \eta_e \tag{3}$$

This function describes the potential energy surface for a fixed θ and χ_A. The five parameters of the generalized Morse function, D_e, β_e, η_e, λ_1, and λ_2, are functions of those two angles. These five parameters are determined for each χ_A and θ from a set of ab initio values of the electronic energy using the nonlinear least-squares method of Levenberg and Marquardt.[64,65] A two-dimensional cubic spline interpolation[63] in θ and χ for these five parameters is performed for general geometries, and replacement in the generalized Morse function furnishes the corresponding potential energy.

The RMOS coordinates for the OH_2 system are either (χ_H, θ, η) or (χ_O, θ, η), where χ_H is the bond angle for the sides OH and HH′, R'_{OH} being the smaller of the two OH distances. We expect the potential energy surface to have a form similar to a Morse function of $\eta - \eta_e$ for each fixed θ and χ_H or χ_O. However, for small values of χ_H or χ_O, below 45°, this is not always the case. Therefore, for bond angles $\chi_O \geq 67.5°$, the coordinates (χ_O, θ, η) are chosen. For $\chi_O < 67.5°$, the coordinates (χ_H, θ, η) are chosen. A spline interpolation over a band near the intersection of these two spaces is used to smooth any discontinuities caused by the separate fittings in these two sets of coordinates.

The geometries for the ab initio calculations were chosen using the RMOS coordinates. For the bond angle χ_H, the values 56.25°, 67.5°, 78.75°, 90°, 112.5°, 135°, 157.5°, and 180° were selected to adequately describe the potential energy surface in the (χ_H, θ, η) coordinates. The LEPS surface[6,10] was used as a guide for selecting the geometries for which ab initio electronic energy calculations were to be performed, as it is a simple empirical PES that has Morse-like behavior for fixed θ and χ_H or χ_O. For the lower of those values of χ_H, the potential energy changed more rapidly with this angle than for the higher ones, necessitating the finer χ_H grid used. The swing angles chosen were $\theta = 0°$, 15°, 30°, 40°, 45°, 50°, 60°, 75°, and 90°. The LEPS surface showed a more rapid change with swing angle in the strong interaction region than away from it, thus the finer grid between 30° and 60°. For some χ_H angles, $\theta = 37°$ and 53° were added. For $\chi_H < 56.25°$, constant values of $\chi_O = 67.5°$, 90°, 112.5°, 135°, 157.5°, and 180° were chosen to adequately describe the PES in the (χ_H, θ, η) coordinates. For this bond angle, a uniform grid was adequate. The corresponding swing angles chosen were $\theta = 0°$, 15°, 30°, 42°, and 45°. Again the LEPS surface displayed a more rapid change with swing angle in the strong interaction region than away from it. For some values of χ_O, $\theta = 39°$ was added. For each pair of constant χ and θ angles, five to seven geometries were selected that represented well the LEPS surface. The configurations specified in this paragraph account for the majority of the ab initio geometries selected.

Other geometries had initially been chosen in the low-χ_H-angle region, at $\chi_H = 22.5°$ and 45° for $\theta = 15°$, 30°, 45°, 60°, and 75°. These points were not used in the fitting procedure but were instead used for the error analysis of the RMOS fitted surfaces. Some additional geometries were chosen to improve the RMOS fit. We restricted the geometries used in the fitting procedure to those with ab initio energies less than 4 eV with respect to the bottom of the isolated H_2 well. This restriction was imposed to improve the fit in regions considered important to the dynamics of the reaction. Several geometries were added to the constant χ, θ sets in the strong interaction region near the dissociation plateau, most of which were used for error analysis. More geometries were chosen to improve the GLDP fit. Any of these geometries that did not correspond to one of the constant χ, θ pairs for the RMOS fit were used for error analysis of the RMOS fitted surfaces.

For a given χ_0 and $R'_{OH'} > R'_{OH}$, no ab initio (χ, θ) set calculations were performed for R'_{OH} 10 b (bohr) and the RMOS potential energy function $V(\chi_0, R'_{OH}, R'_{OH'})$ was taken to be independent of $R'_{OH'}$ for such values of this variable. Similarly, the RMOS $V(\chi_H, R'_{OH}, R'_{HH'})$ was taken to be independent of the largest of $R'_{OH'}$, $R'_{HH'}$ when that quantity exceeded 10 b. Both regular- and high-accuracy ab initio calculations were performed at two collinear configurations for higher internuclear distances, namely, $R'_{HH'} = 1.401$ b, $R'_{OH} = 20.000$ b, $R'_{OH'} = 21.401$ b and $R'_{HH'} = 20.000$ b, $R'_{OH} = 20.000$ b, and $R'_{OH'} = 40.000$ b. These were calculated mainly for calibration purposes and were not used in the RMOS fit but were employed in the GLDP fit.

2.2.2. The GLDP Method. The many-body expansion method of fitting the ab initio data gives a very accurate fit of the data and has a simple mathematical form.[50] It is, however, notorious for generating unphysical features.[45] The resulting fit must be thoroughly examined for spurious wells and barriers resulting from the mathematical form of the fitting function rather than from the ab initio data. We have developed a new method of using virtual points to correct for some of these features. For other regions we have used localized Gaussian functions[66] to remove unphysical features.

The GLDP mathematical form used is the sum of two terms

$$V_{GLDP} = V_{GLEPS} + V_{DPOLY} \tag{4}$$

where the first is a generalized LEPS term, in which a cubic spline fit of near-asymptotic ab initio data for each isolated diatomic molecule is used in place of the Morse function of the usual LEPS function.[67−71] The second term is a sum of two high-order polynomials multiplied by switching functions and corrects the initial GLEPS fit to provide greater accuracy. This term is defined by

$$V_{DPOLY} = S(\mathbf{r}) \sum_{i,j,k} c_{ijk}(r_1 - \bar{r}_1)^i (r_2 - \bar{r}_2)^j (r_3 - \bar{r}_3)^k + S'(\mathbf{r}) \sum_{i,j,k} c'_{ijk}(r_1 - \bar{r}'_1)^i (r_2 - \bar{r}'_2)^j (r_3 - \bar{r}'_3)^k \tag{5}$$

where the c_{ijk} and c'_{ijk} are coefficients, $S(\boldsymbol{r})$ and $S'(\boldsymbol{r})$ are the switching functions, and $r_1 = R'_{OH}$, $r_2 = R'_{OH'}$, and $r_2 = R'_{HH'}$ are the three interatomic distances. Up to ninth-order terms ($i + j + k \leq 9$) are used in the polynomials in eq 5, and the sums extend over all possible sets of i, j, k satisfying this condition. The switching function S is defined by

$$S(\mathbf{r}) = s(b_1)\, s(b_2)\, s(b_3)\, s(b_4)\, t(y_1)\, t(y_2)\, t(y_3) \tag{6}$$

where

$$s(b_i) = \begin{cases} 0, & \text{if } b_i \leq 0; \\ 1, & \text{if } b_i \leq 1; \\ 10b_i^3 - 15b_i^4 + 6b_i^5, & \text{otherwise} \end{cases} \tag{7}$$

in which the b_i for $i = 1-3$ are

$$b_i = (r_i - \bar{r}_{bi})/a_{bi}, \quad i = 1, 2, 3 \tag{8}$$

and

$$b_4 = (a_{b,4,1}w^2 - w + a_{b,4,2})/a_{b,4,3} \tag{9}$$

in which

$$w = \frac{r_1^2 + r_2^2 - r_3^2}{2r_1r_2} \tag{10}$$

The terms $t(y_i)$ are defined by

$$t(y_i) = 1 - \tanh(y_i) \tag{11}$$

where

$$y_i = a_{yi}(r_i - \bar{r}i) \tag{12}$$

The switching function S' is analogous to S with a' and $\bar{r}'$ replacing a and $\bar{r}$, respectively. S and S' are used to turn the two polynomials in V_{DPOLY} on and off in different regions of the PES. The c, c', a, a', $\bar{r}$, and $\bar{r}'$ are variational parameters determined by the fitting procedure. The parameters for S and S' are given in Table 1. For symmetry reasons, a_{b1} and a_{b2}, as well as $\bar{r}_{b1}$ and $\bar{r}_{b2}$, are equal, as are their primed counterparts. The same is true for a_{y1} and a_{y2} and their primed counterparts. The $\bar{r}$ parameters are of the order of small internuclear distances.

The $s(b_i)$ terms in eq 7 force the contribution of one of the two high-order polynomials in V_{DPOLY} in eq 5 to vanish when one of the r_i or the angle between $\boldsymbol{r}_1$ and $\boldsymbol{r}_2$ (χ_O in the RMOS coordinates) reaches a reference value. This is accomplished by the function $s(b_i)$ in eq 7, which varies smoothly from 0 to 1, with continuous first derivatives at $b_i = 0$ and $b_i = 1$. For $i = 1, 2, 3$, $s(b_i)$ approaches zero as r_i approaches the value $\bar{r}_{bi}$, at a rate of decay controlled by a_{bi}. b_4 is a quadratic function of the cosine of the angle between r_1 and r_2. The terms $t(y_i)$ turn the V_{DPOLY} term off for asymptotic geometries. When one r_i reaches its reference value $\bar{r}_i$, $t(y_i) = 0$, and the entire switching function vanishes. This occurs around 3−4 b, as can be seen from the values in Table 1. As a result, the asymptotic regions of the PES have the correct diatomic behavior, included in the V_{GLEPS} term. The slope parameter, a_{yi}, controls how rapidly V_{DPOLY} is made to vanish.

The GLDP form is fitted to the ab initio data using a nonlinear least-squares method to obtain the set of parameters that simultaneously minimize the root-mean-square error and the maximum absolute value deviation from the ab initio data. The unbiased error of the fitted PES is determined with the help of a set of 100 geometries removed at random from the ab initio data and not used in the fitting procedure. Using an initial estimate of the non-linear parameters, the linear parameters, the rms error and the maximum absolute deviation are first determined. The non-linear parameters are then varied until that error and deviation are minimized. New linear parameters are then determined, and the process is continued iteratively until acceptable errors are achieved. The final unbiased errors are then calculated. The resulting PES was examined using equipotential contour plots in the corresponding two-internuclear-distance cartesian space at fixed bond angles as well as equipotential contour plots in hyperspherical coordinates for equatorial views at fixed hyperradii, as discussed in section 3.3. The minimum-energy paths for both the abstraction and exchange reactions were computed as well. These proved to be a very sensitive measure of the smoothness of the surface, able to detect very small irregularities in the low-energy region of the surface. On the basis of these results, new geometries were chosen for ab initio calculations. These geometries were added to the original set of data, and a refitting was performed.

Occasionally, refitting to remove spurious wells was performed using virtual points, defined as geometries for which ab initio data had not been calculated and at which the fitted PES displayed unphysical behavior caused by the form of the fitting function (in particular, the oscillations of the high-order polynomial functions). Energies were assigned to those points so as to eliminate this nonphysical behavior. These virtual point geometries were added to the original data, which was then refit, with the final error analysis performed using only the original ab initio data. Virtual points were not used to judge the accuracy of the new fitted PES. Modifying the degree of the polynomials in order to remove unphysical features of the surface can be difficult, since it is not clear which terms in the polynomials cause these features, and this can also cause other unphysical features to arise in other regions. Virtual points are a tool that goes directly to the source of the problem: lack of sufficient data to produce a physically correct fitting of the PES in all regions of interest. The introduction of these points permits the use of physical insight for regions for which ab initio data is not available, without biasing the regions for which data is available, as they do not change the fitting in regions removed from the problem area. As a result, the use of virtual points furnishes an improved fitting procedure that decreases the shortcomings of the mathematical form of the fitting function. They do not bias the effect of the ab initio points since they are not used to determine the fitting accuracy of the final PES, and can be considered as equivalent to fitting parameters.

TABLE 1: GLDP Switching Function Parameters[a]

parameter	$^3A'$ S	$^3A'$ S'	$^3A''$ S	$^3A''$ S''
$\bar{r}_{b1}$, b	1.26	1.26	1.28	1.28
a_{b1}, b	0.04	0.04	0.04	0.04
$\bar{r}_{b2}$, b	1.26	1.26	1.28	1.28
a_{b2}, b	0.04	0.04	0.04	0.04
$\bar{r}_{b3}$, b	0.71	0.60	0.76	1.06
a_{b3}, b	0.10	0.23	0.10	0.26
$a_{b,4,1}$	−0.09	0.00	0.07	0.00
$a_{b,4,2}$	1.43	1.01	1.25	0.778
$a_{b,4,3}$	1.44	1.74	1.51	1.24
$\bar{r}_1$, b	2.91	2.90	3.37	2.93
a_{y1}, b^{-1}	1.95	1.49	1.39	2.60
$\bar{r}_2$, b	2.91	2.90	3.37	2.93
a_{y2}, b^{-1}	1.95	1.49	1.39	2.60
$\bar{r}_3$, b	3.71	2.98	4.04	3.31
a_{y3}, b^{-1}	0.97	1.03	1.39	1.27

[a] These parameters are used for S and S', in the latter of which the parameters are primed, as described in eqs 5−12.

Not always were virtual points sufficient to remove unphysical features. For regions of the PES along the minimum-energy path, and for regions for which the system's configuration is slightly bent, we found it more helpful to use localized Gaussian functions[66] of the form

$$\Delta V = c_E e^{-[(R'_{OH}-R'_{OH,e})^2/2d^2{}_{OH}+(R'_{HH'}-R'_{HH',e})^2/2d^2{}_{HH'}+(\chi_H-\chi_{H,e})^2/2d^2{}_{\chi H}]} \tag{13}$$

(with equivalent forms for the coordinates R'_{OH}, R'_{OH}, and χ_O) to remove unphysical features of the fitted PES. The values $R'_{OH,e}$, $R'_{HH',e}$, and $\chi_{H,e}$ determine the location of the maximum of the Gaussian, d_{OH}, $d_{HH'}$, and $d_{\chi H}$ are measures of the width of the Gaussian, and c_E is the value of the Gaussian at its maximum. These parameters were chosen carefully to remove some unphysical features. It was often necessary to place two or three Gaussians in close proximity to each other to remove a broader, small feature without disturbing the surrounding regions.

Localized Gaussians were particularly helpful in the description of the van der Waals well region. Ab initio data in this region produced a well depth of 0.2 kcal/mol. The GLDP fit had resulted in a larger well depth initially and was corrected to furnish 0.2 kcal/mol using localized Gaussians. The RMOS fit did not consider the van der Waals region, as these ab initio geometries were not usable with the RMOS fitting procedure.

The regular-accuracy surfaces were created by subtracting the fitted correction surface from the fitted high-accuracy PES. This avoids an additional fitting and gives consistent results. For large values of the interatomic distances, the fitted high- and regular-accuracy RMOS PESs were subject to the constraints described in the last paragraph of section 2.2.1, owing to the lack of constant (χ, θ) sets of data in that region. A similar constraint was imposed on the regular-accuracy GLDP fitted PES. The high-accuracy GLDP fit, however, uses all of the data, including the energies of the two stretched geometries described in that paragraph. The complete set of data is generated from all of the ab initio regular-accuracy results by adding to them the fit to the correction surface, as described in section 2.2.3.

The resulting GLDP PESs for the regular-accuracy and high-accuracy data for both the $^3A'$ and $^3A''$ surfaces are compared to the corresponding RMOS PESs and to the LEPS one in section 3.3.

2.2.3. The Correction Surface. This surface is produced by fitting the differences between the ab initio high-accuracy and regular-accuracy calculations for the 112 geometries used in the high-accuracy electronic energy calculation. These geometries were chosen on the basis of an initial RMOS fit to the regular-accuracy data. Examination of the saddle-point energies for the different χ_H and χ_O constant bond angle equipotential contour plots determined the three most important values of each of these two angles needed to represent the corresponding saddle-point regions. The values were 67.5°, 112.5°, and 180° for both χ_H and χ_O. Further plotting of the RMOS energies along cuts transverse to the saddle-point minimum-energy path for the collinear configurations furnished the initial geometries for the high-accuracy electronic energy calculations. For each of these transverse cuts, the saddle-point geometry and geometries halfway down each side of the barrier were chosen. For each minimum-energy path, geometries halfway down the barrier and geometries near the asymptotic region were chosen. After calculations at these geometries and initial fitting of the correction surface were performed, other geometries at these fixed bond angles were chosen to improve the fit. Differences between the ab initio high-accuracy and regular-accuracy data were in the range of 3.8−4.8 kcal/mol. This method of taking a straight difference of the two values produced significant differences even in the asymptotic O + H + H region and was considered undesirable. However, when the two sets of data were adjusted separately for a zero of energy at an asymptotic O + H + H geometry, their differences decreased to the range 0.25−1.1 kcal/mol. The smaller range of the correction energies made possible a more accurate fit to the data. After the correction surface was added to the regular-accuracy ab initio data, the zero of energy was placed at the bottom of the H_2 well for use in comparison with other surfaces. This final adjustment does produce some negative differences between the final high-accuracy and regular-accuracy PESs, even though the ab initio differences are always positive as expected for a variational procedure. Nevertheless, this is the most appropriate way of correcting the regular- and high-accuracy calculations for differences in the zero of energy.

The correction surface itself consists of three diatomic correction terms and one global triatomic correction term

$$\mathrm{V_C} = P_{\mathrm{OH}} + P_{\mathrm{HH'}} + P_{\mathrm{OH'}} + T_{\mathrm{OHH'}} \tag{14}$$

The diatomic terms are one-dimensional cubic polynomials

$$P_{\mathrm{AB}} = c_{\mathrm{AB}} S_{\mathrm{AB}} \sum_{i=0}^{3} a_i^{\mathrm{AB}} R'^{i}_{\mathrm{AB}} \tag{15}$$

The triatomic term is a global third-degree polynomial in three variables

$$T_{\mathrm{OHH'}} = \sum_{i,j,k=0}^{3} \alpha_{ijk} \bar{R}'^{\,i}_{\mathrm{OH}} \bar{R}'^{\,j}_{\mathrm{HH}} \bar{R}'^{\,k}_{\mathrm{OH}} \tag{16}$$

where

$$\bar{R}'_{\mathrm{AB}} = R'_{\mathrm{AB}} - R'_{\mathrm{e,AB}} \tag{17}$$

and $i + j + k \leq 3$. The R'_{AB} are the interatomic distances, and $R'_{e,AB}$ are the equilibrium interatomic distances. S_{AB} is a Heaviside function used to cut off the effect of the diatomic terms at a distance of 10 b. The constants c_{OH} and $c_{OH'}$, the equilibrium distances $R'_{e,OH}$ and $R'_{e,OH'}$, and the constants á$_{ijk}$ and á$_{kji}$ are equal for symmetry reasons. The diatomic correction terms make necessary the calculation of diatomic energies. Electronic energy calculations at eight geometries for the OH diatom and nine geometries for the H_2 diatom were performed. These were fitted using the diatomic term P_{AB} of eq 15 with the Levenberg−Marquardt method of least-squares fitting.[64,65] The constants c_{AB} were chosen as 0.3 for the OH diatom and 0.7 for the H_2 diatom to produce the correct ab initio correction value at the saddle point. This choice of constant multipliers left a small positive value of the correction for all data to be fitted by the triatomic term of eq 16. Subtracting the diatomic correction terms from V_C without including these constants resulted in some negative values that would have to be fitted by that triatomic term, as well as some positive ones. This is difficult to achieve without introducing spurious features. The effect of the diatomic polynomials is eliminated at large bond distances by the Heaviside function S_{AB}, resulting in small positive values for the remaining triatomic correction term. The remainder of the difference between the high- and regular-accuracy calculations was fitted using $T_{OHH'}$ in eq 17 with the Levenberg−Marquardt fitting method. The final fitted correction surface was added to the regular-accuracy ab initio electronic structure energies at all 951 geometries to raise their accuracy to that of the 112 high-accuracy energies.

Several other mathematical forms were initially considered for fitting the correction surface in addition to the one just described. Truhlar and co-workers[72] had used a correction surface to improve specific areas of potential energy surfaces for the $OH + CH_4 \rightarrow H_2O + CH_3$ and $CF_3 + CD_3H \rightarrow CF_3H + CD_3$ reactions. We were, however, interested in improving the entire surface, using a smooth mathematical form. Gaussian and other mathematical forms that tend toward zero asymptotically were ruled out since the correction surface does not tend toward zero or to another constant at large interatomic distances. Asymptotically, the correction for the H_2 molecule approaches 0.8 kcal/mol, and the correction for OH approaches 0.3 kcal/mol. The discrepancies in these corrections are due primarily to the incomplete basis sets used for the regular-accuracy calculation and, to a lesser extent, to an incomplete treatment of electron correlation.

Another mathematical form suggested itself when the ab initio high-accuracy data and their correction values were displayed in equipotential contour plots of the regular-accuracy surface. This allowed better visualization of the correction surface. For each of the three fixed χ_H bond angles, the correction increased smoothly with swing angle from 0.3 to 0.8 kcal/mol. For the three fixed χ_O bond angles, the correction increased smoothly with bond angle from 0.8 kcal/mol to their saddle-point value for that bond angle. This suggested using a function of the swing angle that could incorporate most of the correction, and then a global term to represent the remainder. A spline interpolation was used for the swing angle term. There were enough ab initio

TABLE 2: Ab Initio $O(^3P) + H_2$ Energetics for Special Geometries[a]

structure	aug-cc-pVTZ (hartree)	aug-cc-pVQZ (hartree)	aug-cc-pV5Z (hartree)
O−H−H[b]	−76.118 72 (−0.127 44)	−76.137 23(−0.146 67)	−76.143 49 (−0.153 15)
$O + H_2$	−76.142 16 (−0.149 49)	−76.160 09(−0.168 02)	−76.166 18 (−0.174 30)
OH + H	−76.136 51 (−0.143 03)	−76.156 05(−0.163 22)	−76.162 62 (−0.170 00)
O + H + H[c]	−75.971 15 (0.023 33)	−75.988 12 (0.005 86)	−75.993 92 (−0.000 11)

[a] The numbers in parentheses are ICCI+Q (ICCI values with the Davidson correction) and a shift of +76. [b] Saddle-point configuration. [c] Separated atom configuration.

TABLE 3: $O(^3P) + H_2$ Saddle-Point and Asymptotic Configuration Energetics

	aug-cc-pVTZ (kcal/mol)	aug-cc-pVQZ (kcal/mol)	aug-cc-pV5Z (kcal/mol)	ebs[a] (kcal/mol)	exptl (kcal/mol)
			ICCI		
E_b[b]	14.7	14.3	14.2	14.1	
D_eOH	103.8	105.4	105.9	106.3	106.6
D_eHH	107.3	107.9	108.1	108.3	109.5
			ICCI+Q		
E_b[b]	13.8	13.4	13.3	13.2	
D_eOH	104.4	106.1	106.6	107.0	106.6
D_eHH	108.4	109.1	109.3	109.4	109.5

[a] Extrapolation to the basis set limit of the aug-cc-pVnZ results ($n = T, Q, 5$). [b] Barrier height for the $O(^3P) + H_2 \rightarrow H + OH$ reaction.

correction data for each fixed bond angle to expect a good fit from this interpolation without unphysical features. For the global term, a low-order three-dimensional polynomial as in eq 16 was expected to provide a good fit. Both cubic and quartic polynomials were fit to the remaining correction using the Levenberg−Marquardt method,[64,65] with the cubic polynomial giving better results than the quartic one. However, this mathematical form was not chosen for reasons discussed later in section 3.2.

2.3. Minimum-Energy Path. The collinear minimum-energy paths used to evaluate the fitted surfaces were determined using the method of steepest descent.[73] The gradient of the potential energy is followed in the direction of the negative eigenvalue of the Hessian starting at the saddle-point configuration.[74,75] This process is repeated for the opposite side of the barrier to give the full minimum-energy path. The saddle-point itself is determined by following the gradient from an initial guess to the position on the PES where the gradient is zero in all directions and the Hessian has one negative eigenvalue. This path is invariant with the choice of coordinate systems.[73] We have used the Jacobi mass-scaled coordinates defined in section 3.2 below. Usually, a fine spacing of steps along the MEP (0.01 b) gave a reasonable representation of the MEP. However, small wells in the fitted PES, of the order of 0.2 kcal/mol, can result in a malfunction of the steepest descent algorithm with this fine step size. A simple doubling of the step size to 0.02 b often corrected this problem. In addition, if a PES is not smooth at a high magnification (0.01 b), the resulting MEP will not be smooth. Also in this case, increasing the step size results in a smoother MEP. For example, the RMOS PES involves linear interpolations over θ every 1°, producing a PES that is not smooth on the 0.01 b scale. To achieve a smooth MEP, a step size of 0.05 b was required. As a result, the saddle-point region is not as well-defined as when a 0.01 b step size suffices. Plots of the energy along the MEP for each of the PESs developed here are discussed below.

3. Results and Discussion

3.1. Electronic Energy. Table 2 gives the ab initio energetics for the $O(^3P) + H_2$ reaction at the reactants, products, abstraction saddle point, and separated atom configurations for the aug-cc-pVTZ, aug-cc-pVQZ, and aug-cc-pV5Z basis sets. The numbers in parentheses are the ICCI+Q (Davidson-corrected ICCI) values, with an upward shift of 76 hartree. Since that saddle point has a collinear geometry, it is the same for the $^3A'$ and $^3A''$ states. Using these data, these energies were extrapolated to the basis set limit by a Martin−Schwartz three-point extrapolation method.[76] The corresponding results for the ICCI and ICCI+Q calculations are given in Table 3. From that table we see that the extrapolated D_e's of OH and H_2 are 106.3 and 108.3 kcal/mol for ICCI and 107.0 and 109.4 kcal/mol for ICCI+Q, respectively, compared to 106.6 and 109.5 kcal/mol from experiment. Because the calculations were done for an OH_2 supermolecule, only the Davidson-corrected[58] values are reliable for H_2, and indeed the extrapolated D_e is within 0.1 kcal/mol of experiment. For OH the calculated D_e's are 0.3 kcal/mol too small for ICCI and 0.4 kcal/mol too large for ICCI+Q. This suggests that the multireference Davidson correction slightly overestimates the effect of higher excitations. The extrapolated barrier heights for the O−H−H saddlepoint are 14.1 and 13.2 kcal/mol for the ICCI and ICCI+Q calculations, respectively. There are no experimental numbers for the barrier height. However, Peterson and Dunning[77] obtained 13.2 kcal/mol, in good agreement with our results, using a very similar wave function (their ext-CAS+1+2+Q) and basis set. (They used the full aug-cc-pVnZ basis sets, whereas we used even-tempered functions as discussed above.) The ICCI+Q results with the aug-cc-pV5Z basis set are very close to the extrapolated values. The D_e's for OH and H_2 at this level of calculation (without basis set extrapolation) differ from experiment by no more than 0.2 kcal/mol, and the barrier height is within 0.1 kcal/mol of the extrapolated value. Thus, the aug-cc-pV5Z results are within chemical accuracy and appear to be accurate to within a few tenths of a kcal/mol. As discussed below, these results (denoted as high accuracy) were used to calibrate the surface, while the regular accuracy was used to generate the global PES. For the regular-accuracy calculations, the abstraction barrier height is 0.1 kcal/mol higher, the H_2 D_e is 0.2 kcal/mol smaller, and the OH D_e is 0.5 kcal/mol smaller than the high-accuracy results.

Tables 4, 5, and 6 give the results of regular- and high-accuracy ab initio calculations for OH, H_2, and $O(^3P) + H_2$ PES, respectively. They were used to develop a correction term to convert the regular-accuracy energies to high-accuracy ones. The starting point is the correction for the diatomic terms using

TABLE 4: OH Diatomic Data

	regular accuracy			high accuracy			
R (b)	ICCI (hartree)	ICCI+Q[a] (hartree)	Δ*E*[b] (kcal/mol)	ICCI (hartree)	IC CI+Q[a] (hartree)	Δ*E*[b] (kcal/mol)	ΔΔ*E*[c] (kcal/mol)
10.0	−75.488 18	−0.494 20	0.0	−75.493 94	−0.500 12	0.0	0.00
5.0	−75.490 58	−0.496 72	−1.58	−75.496 40	−0.502 71	−1.63	0.05
4.0	−75.501 64	−0.508 17	−8.77	−75.507 66	−0.514 38	−8.95	0.18
3.0	−75.552 99	−0.560 28	−41.47	−75.559 43	−0.566 96	−41.94	0.47
2.5	−75.602 12	−0.60 952	−72.36	−75.608 82	−0.616 46	−73.00	0.64
1.83	−75.655 63	−0.662 77	−105.78	−75.662 63	−0.670 00	−106.60	0.82
1.6	−75.637 10	−0.644 09	−94.06	−75.64 422	−0.651 44	−94.95	0.89
1.4	−75.570 62	−0.577 49	−52.27	−75.577 96	−0.585 03	−53.28	1.01

[a] ICCI results with a Davidson correction and a shift of +76. [b] Differences between the ICCI value at *R* and the ICCI value at 10.0 b. [c] Differences between the regular- and high-accuracy Δ*E*.

TABLE 5: H_2 Diatomic Data

	regular accuracy		high accuracy		
R (b)	ICCI+Q[a] (hartree)	Δ*E*[b] (kcal/mol)	ICCI+Q[a] (hartree)	multicolumn1cΔE[b] (kcal/mol)	ΔΔ*E*[c] (kcal/mol)
10.0	−0.999 90	0.0	−1.000 00	0.0	0.00
5.0	−1.003 47	−2.24	−1.003 65	−2.29	0.05
4.0	−1.015 84	−10.00	−1.016 17	−10.15	0.15
3.0	−1.056 59	−35.57	−1.057 08	−35.82	0.25
2.5	−1.093 17	−58.53	−1.093 70	−58.80	0.27
2.0	−1.137 33	−86.24	−1.137 91	−86.54	0.30
1.4	−1.173 58	−108.99	−1.174 23	−109.33	0.34
1.2	−1.16396	−102.95	−1.164 66	−103.33	0.38
1.0	−1.12344	−77.52	−1.124 23	−77.96	0.44

[a] ICCI results with a Davidson correction and a shift of +76. [b] Differences between the ICCI value at *R* and the ICCI value at 10.0 b. [c] Differences between the regular- and high-accuracy Δ*E*.

TABLE 6: OHH High-Accuracy Data

	regular accuracy		high accuracy		
structure	ICCI+Q[a] (hartree)	Δ*E*[b] (kcal/mol)	ICCI+Q[a] (hartree)	Δ*E*[b] (kcal/mol)	ΔΔ*E*[c] (kcal/mol)
O + H + H[d]	0.005 86	0.0	−0.000 11	0.0	0.00
O + H_2	−0.167 78	−108.96	−0.174 30	−109.31	0.35
OH + H	−0.162 73	−105.79	−0.170 00	−106.61	0.82
O − H − H[e]	−0.146 17	−95.4	−0.153 15	−96.03	0.63

[a] ICCI results with a Davidson correction and a shift of +76. [b] Differences between the ICCI+Q result and its value for O + H + H. [c] Differences between the regular- and high-accuracy Δ*E*. [d] Separated atom configuration. [e] Saddle-point configuration.

the data in Tables 4 and 5, which is then modified by a three-body term. Taking the O + H + H asymptote (separated atoms) as the zero of energy makes this three-body correction term positive over the entire surface.

As discussed by Walch,[78] the amount of negative ion (O^-) character in the O(^{3}P) + H_2 reaction is larger at the saddle point than at the reactants or products. Thus, it is important to use basis functions and a CASSCF wave function that can describe the electron affinity (EA) of oxygen. More recently Kendall et al.[79] did a systematic study of the EA of the first-row atoms. For O they found that addition of diffuse functions to the cc-pVQZ basis set increased the EA by 0.451 eV for diffuse sp functions, by 0.029 eV for diffuse d functions, by 0.019 eV for diffuse f functions, and by 0.019 eV for diffuse g functions. Thus, at least diffuse sp functions are required for O(^{3}P) + H_2 and diffuse d functions were also added in our calculations. The same authors also found that a Hartree−Fock reference wave function gave an EA for O of 1.060 eV, but going to a CAS(2p,2p′) reference wave function gave 1.347 eV compared to 1.401 eV for a full CI calculation (all with the aug-cc-pVQZ basis set). This is the reason for including a 2p′ shell in our calculations. We found that only the 2p′ orbital corresponding to the doubly occupied O2p orbital had to be included (for ICCI+Q). Omitting this orbital increases the barrier height for O(^{3}P) + H_2 by 0.6 kcal/mol. Adding the 2p′ orbitals corresponding to the singly occupied O2p orbitals had less than a 0.1 kcal/mol effect on this height. We also tried the method of coupled-cluster single and double excitation with a perturbational estimate of triple excitation (CCSD(T)) and found that this gave the same barrier height as did ICCI (using the aug-cc-pVQZ basis set). However, the ICCI barrier height with this basis set is 0.9 kcal/mol higher than for ICCI+Q, which in turn is much closer to the best estimate from experiment.

Two other sources of error that must be taken into account are the effects of core valence (CV) correlation and spin−orbit interactions. The CV effect arises from correlating the O1s shell, which was kept frozen in all the other calculations reported here. The calculation with the correlated O1s shell requires the use of basis sets that were developed for this purpose.[80] (These basis sets include additional functions for correlating the inner shell.) The CCSD(T) method was used for these correlated calculations. The results obtained for OH are given in Table 7 as a function of R'_{OH}. It is seen that at the OH equilibrium distance of 1.835 b the CV effect increases D_e by 0.14 kcal/mol. This effect, however, rapidly decreases as R'_{OH} increases. In fact, at the saddle point (R'_{OH} = 2.314 b), the CV effect decreases the barrier height by only 0.01 kcal/mol. Thus, the CV effect on the potential energy surface is mainly a small (0.15 kcal/mol)

TABLE 7: Core-Valence Effect for OH

R'_{OH} (b)	ΔE^a (kcal/mol)
2.2	0.00
2.0	0.08
1.835	0.14

[a] The net change in energy produced by the core-valence effect.

TABLE 8: Correction Surface Error Analysis

error (kcal/mol)	$^3A''$	$^3A'$
rms	0.058	0.059
max[a]	0.14	0.15

[a] Maximum absolute value error.

lowering of the OH + H asymptote with respect to reactants. This effect is of the same order as the estimated error in the high-accuracy calculations. Our values for the CV effect are in good agreement with the results of Peterson and Dunning.[77]

Spin−orbit interactions can, in general, have a significant effect on the system's barrier heights.[81−86] However, for the OH_2 system, the ^{3}P state of the O atom is split into three components: $^3P_2$, $^3P_1$, and $^3P_0$. $^3P_2$ is the lowest one, and the $^3P_1$ and $^3P_0$ states are 0.45 and 0.65 kcal/mol higher, respectively.[87] However, it has been pointed out[18] that all five components of the $^3P_0$ state correlate with the ^{3}P surface of OHH, but only one component of the $^3P_1$ state does so, and no components of $^3P_2$ do. Thus the ^{3}P surface of OHH correlates with the $^3P_0$ and $^3P_1$ states of the O atom, and these states are split by only 0.2 kcal/mol. Once again this effect is within the estimated accuracy of the ab initio calculations.

3.2. Correction Surface. The spline swing angle fitting form resulted in a good overall fit to the correction surface with a root-mean-square error of 0.15 kcal/mol for both the $^3A'$ and $^3A''$ states. However, it gave a large maximum absolute value error. In the saddle-point regions, this spline form was unable to reproduce occasional deviations from the usually smoothly increasing correction term. This left negative values, in areas surrounded by small positive values, for the global triatomic cubic polynomial function to describe. The low-order polynomials were unable to fit these negative areas without higher order terms that would have themselves produced spurious features in the surface.

The diatomic polynomial fitting method gave better results than the spline swing angle approach. The corresponding $T_{OHH'}$ term in eq 14 did not have to describe negative wells. The small positive values left after subtracting the diatomic terms P_{AB} were well-represented with the global cubic polynomial $T_{OHH'}$. This fitting method was chosen owing to the resulting improved root-mean-square deviation and much smaller maximum absolute value deviation. Table 8 displays the results of the error analysis for the $^3A''$ and $^3A'$ surfaces. The fitted correction surface has a root-mean-square error with respect to the ab initio data of 0.058 kcal/mol for the $^3A''$ state and 0.059 kcal/mol for the $^3A'$ state. The maximum absolute value deviation from the ab initio data is 0.14 kcal/mol for the $^3A''$ state and 0.15 kcal/mol for the $^3A'$ state. Both surfaces are smooth over the entire region spanned by the regular-accuracy ab initio data.

Plots of these surfaces in kinematic-rotation-invariant hyperspherical coordinates using an equatorial projection afford the best information for reactive scattering calculations using these coordinates. The interatomic distances are first transformed into the Jacobi coordinates $\mathbf{R}'_{C'}$, $\mathbf{r}'_C$, and γ_C depicted in Figure 3. These coordinates are then mass-scaled according to[88−91]

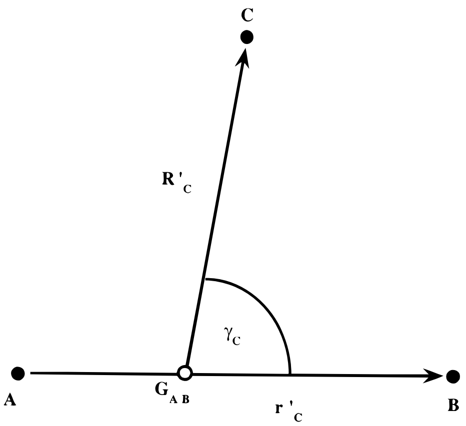

Figure 3. Jacobi coordinates. The diagram depicts the Jacobi coordinates R'_C, r'_C, and γ_C for a general ABC system. G_{AB} is the center of mass of diatom AB, and γ_C is in the 0−π range.

$$\mathbf{R}_C = a_C \mathbf{R}'_C, \quad \mathbf{r}_C = a_C^{-1} \mathbf{r}'_c, \quad a_C = (\mu_{C,AB}/\mu_{AB}) \qquad (18)$$

where μ_{AB} is the reduced mass of AB and $\mu_{C,AB}$ is the reduced mass of the C, AB pair. A set of spherical polar coordinates[92,93] are defined as the hyperradius ρ, and the angles γ_C and ω_C

$$\rho = (R_C^2 + r_C^2)^{1/2} \qquad (19)$$

$$\gamma_C = \left(\frac{\mathbf{R}_C \cdot \mathbf{r}_C}{r_C R_C}\right); \quad 0 \le \gamma_C \le \pi \qquad (20)$$

$$\omega_C = 2\arctan\left(\frac{r_C}{R_C}\right); \quad 0 \le \omega_C \le \pi \qquad (21)$$

The corresponding internal configuration space Cartesian coordinates are defined by

$$X_C = \rho \sin \omega_C \cos \gamma_C \qquad (22)$$

$$Y_C = \rho \sin \omega_C \sin \gamma_C \qquad (23)$$

$$Z_C = \rho \cos \omega_C \qquad (24)$$

The coordinates we use for Figures 4 and 5 correspond to a projection or mapping of the points of a constant ρ hemisphere onto a plane tangent to it at the point the Y_C axis intersects that hemisphere. This projection[93] is defined as follows. We first introduce the kinematic-rotation-invariant internal hyperangles ϑ_C and φ_C related to ω_C, γ_C by

$$\cos \vartheta_C = \sin \omega_C \sin \gamma_C; \quad 0 \le \vartheta_C \le \frac{\pi}{2} \qquad (25)$$

$$\sin \vartheta_C \sin \varphi_C = \sin \omega_C \cos \gamma_C \qquad (26)$$

$$\sin \vartheta_C \cos \varphi_C = \cos \omega_C; \quad 0 \le \vartheta_C < 2\pi \qquad (27)$$

The Cartesian coordinates x_C, y_C of the point on this tangent plane onto which the point (X_C, Y_C, Z_C) on the hemisphere is mapped are defined by

$$x_C = \rho \vartheta_C \cos \varphi_C \qquad (28)$$

$$y_C = \rho \vartheta_C \sin \varphi_C \qquad (29)$$

This mapping of the PES onto this plane is called the equatorial view because it is a projection of the hemisphere on a plane

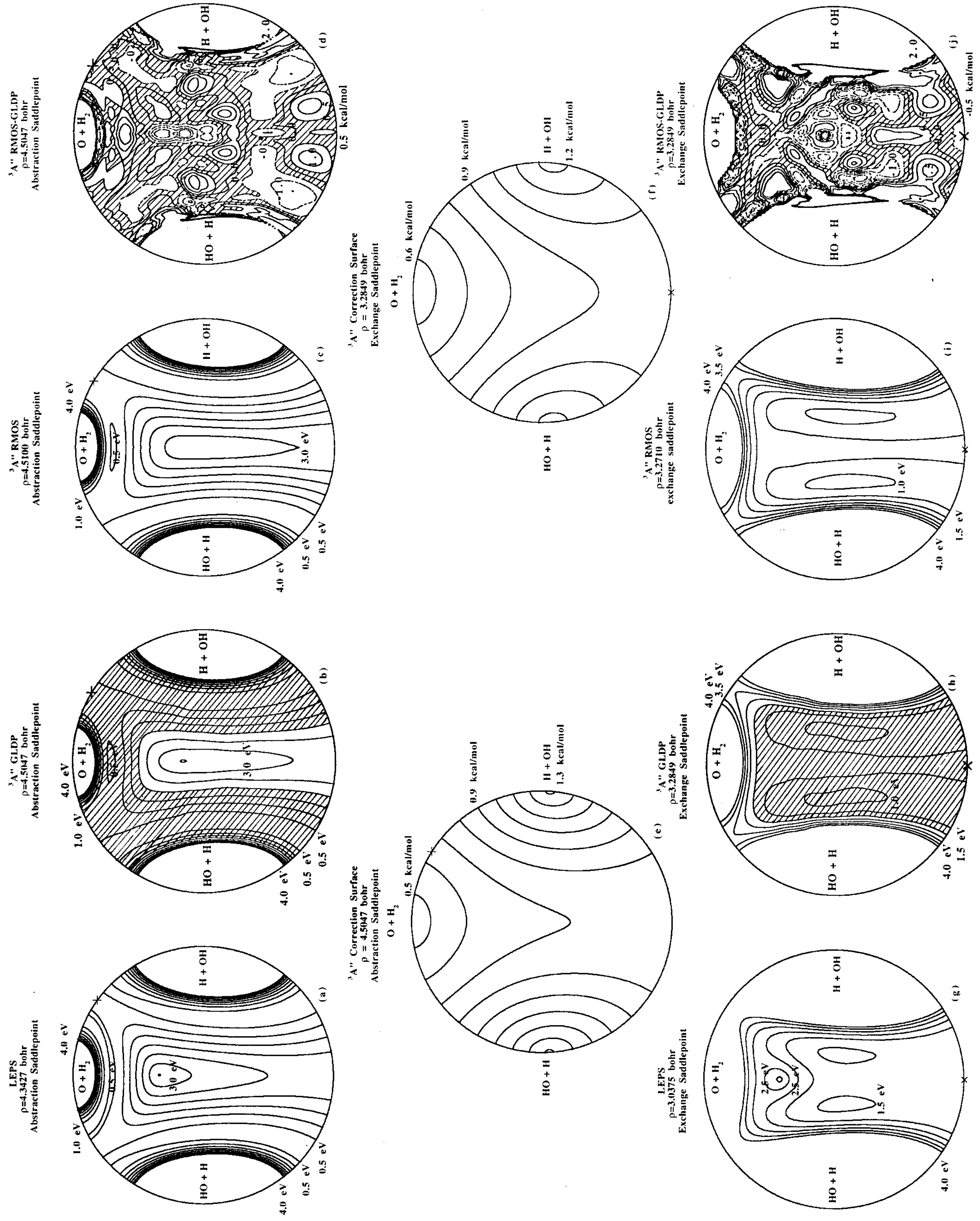
LEPS
ρ=4.3427 bohr
Abstraction Saddlepoint
O + H2
HO + H
H + OH
1.0 eV
4.0 eV
3.0 eV
0.5 eV
4.0 eV
0.5 eV
0.5 eV
(a)
³A" GLDP
ρ=4.5047 bohr
Abstraction Saddlepoint
O + H2
HO + H
H + OH
1.0 eV
4.0 eV
3.0 eV
4.0 eV
0.5 eV
0.5 eV
(b)
³A" RMOS
ρ=4.5100 bohr
Abstraction Saddlepoint
O + H2
HO + H
H + OH
1.0 eV
4.0 eV
0.5 eV
3.0 eV
4.0 eV
0.5 eV
0.5 eV
(c)
³A" RMOS-GLDP
ρ=4.5047 bohr
Abstraction Saddlepoint
O + H2
HO + H
H + OH
2.0
-1.0
0.5 kcal/mol
(d)
³A" Correction Surface
ρ = 4.5047 bohr
Abstraction Saddlepoint
O + H2
HO + H
H + OH
0.5 kcal/mol
0.9 kcal/mol
1.3 kcal/mol
(e)
³A" Correction Surface
ρ = 3.2849 bohr
Exchange Saddlepoint
O + H2
HO + H
H + OH
0.6 kcal/mol
0.9 kcal/mol
1.2 kcal/mol
(f)
LEPS
ρ=3.0375 bohr
Exchange Saddlepoint
O + H2
HO + H
H + OH
2.5 eV
2.5 eV
1.5 eV
4.0 eV
(g)
³A" GLDP
ρ=3.2849 bohr
Exchange Saddlepoint
O + H2
HO + H
H + OH
4.0 eV
3.5 eV
1.0 eV
4.0 eV
1.5 eV
(h)
³A" RMOS
ρ=3.2710 bohr
exchange saddlepoint
O + H2
HO + H
H + OH
4.0 eV
3.5 eV
1.0 eV
4.0 eV
1.5 eV
(i)
³A" RMOS-GLDP
ρ=3.2849 bohr
Exchange Saddlepoint
O + H2
HO + H
H + OH
2.0
-1.0
-0.5 kcal/mol
(j)

tangent to it at the point on its equator defined by $\omega_C = \gamma_C = \pi/2$. It permits viewing all three arrangement channel regions (for which two of the atoms are closer to each other than to the third one) as well as regions for which the distances between all three atoms are of the same order, for a given value of the hyperradius ρ. In Figures 4 and 5, atom C is O. For each plot, the $O + H_2$ arrangement region is at the top, and the two symmetric H + OH regions are on the left and right. The circle at the edge of each plot represents collinear configurations. The equipotentials in the arrangement channel regions cover a wide range of γ. For a given surface, as the system moves toward an asymptotic configuration, the energy remains nearly constant with respect to γ_C. For the $O + H_2$ system, the vertical line through the center of the plot is a symmetry line.

Figures 4e and 5e display equatorial views of the $^3A''$ and $^3A'$ correction surfaces for the abstraction saddle-point hyperradius. The saddle point, denoted by +, has a correction of 0.64 kcal/mol. The correction energy varies smoothly from slightly below 0.5 kcal/mol in the $O + H_2$ arrangement channel region to 1.3 kcal/mol in the corresponding H + OH arrangement channel region. The correction changes more rapidly as one approaches the H + OH channel configuration. Near arrangement configurations, the energy is nearly constant with respect to γ_C. The $^3A'$ correction surface has similar characteristics to the $^3A''$ one, but with slightly higher values overall. The equatorial views of the $^3A''$ and $^3A'$ correction surfaces for the exchange saddlepoint hyperradius given in Figures 4f and 5f show the same behavior as for the abstraction hyperradii, again with a higher overall energy for the $^3A'$ correction surface as compared to the $^3A''$ one. The exchange saddle point, denoted by ×, has a correction of 0.95 kcal/mol. The correction surface no longer changes more rapidly when approaching the H + OH arrangement channel configuration. For a given surface, the correction for the exchange saddle-point hyperradius is higher than for the abstraction saddle-point hyperradius.

3.3. Comparison of the RMOS, GLDP, and LEPS Potential Energy Surfaces. Table 9 gives results of the error analysis for the GLDP regular-accuracy, GLDP high-accuracy, and RMOS high-accuracy surfaces for the $^3A'$ and $^3A''$ states. The two $^3A''$ GLDP surfaces have root-mean-square (rms) errors of 0.27 kcal/mol, with maximum absolute value deviations of 0.39 kcal/mol. These errors are calculated using a subset of 100 ab initio randomly chosen geometries not used in the fitting procedure. The errors for the $^3A'$ GLDP surfaces are very similar to the $^3A''$ ones, having a rms error of 0.28 kcal/mol with a maximum absolute value deviation of 0.38 kcal/mol. The fitting procedure for the GLDP minimized the maximum absolute value deviation as well as the rms error. As a result, the maximum absolute value deviation is within 0.1 kcal/mol of the rms error. The RMOS surfaces have a rms error of 0.42 kcal/mol for $^3A''$ and 0.53 kcal/mol for $^3A'$. The maximum absolute value deviations are 2.38 kcal/mol for the $^3A''$ RMOS surface and 2.44 kcal/mol for the $^3A'$ RMOS surface. These deviations are not controlled in this fitting procedure. The error analysis for the RMOS surfaces are based on the ab initio data that was unusable for the RMOS fitting method. These include geometries initially calculated in the low χ_H angle region, at $\chi_H = 22.5°$ and $\chi_H = 45°$ for $\theta = 15°$, 30°, 45°, 60°, and 75° and all geometries calculated for the GLDP surface that did not correspond to the selected χ, θ of the RMOS fit. The RMOS fitting procedure forced the generalized Morse curves to pass through all ab initio points at the preselected θ, χ for all but 8 of the 120 θ, χ pairs of values. Because only 5 points per θ, χ were chosen for these 112 θ, χ cuts, and the generalized Morse function has 5 parameters, no error minimization was performed. For the other eight cuts more than five points were chosen to improve the fitted surface. For those, an error minimization fit was performed. The significantly larger maximum absolute deviations observed for the RMOS fit compared to the GLDP one occur in the repulsive regions of the Morse function. A slight deviation of the Morse shape from the correct one in this region can cause a large deviation in the energy. The rms error for the GLDP fit is 0.15 kcal/mol lower than for the RMOS fit for the $^3A''$ surface and 0.25 kcal/mol lower for the $^3A'$ surface, which is nearly as much as the GLDP error itself. The maximum deviations have larger discrepancies, with nearly a six-fold difference between GLDP and RMOS.

In Figure 4 we compare the GLDP, RMOS, and LEPS surfaces for the $^3A''$ state. Here, the LEPS surface was chosen for comparison as it was originally used in the selection of ab initio geometries. The plots are equatorial views of equipotential contours of the PESs at constant values of the hyperradius ρ, as defined in section 3.2. Panel a displays the LEPS surface for the abstraction saddle point ρ. The saddle point is indicated by a + on the upper right side of the plot. Panel b depicts the GLDP high-accuracy surface at its abstraction saddlepoint $\rho = 4.5047$ b, and panel c shows the RMOS surface at its abstraction saddle point $\rho = 4.5100$ b. Again the saddle point is marked by a +. All three have similarly shaped equipotential contours, with the LEPS PES differing more from the GLDP surface than the RMOS one does. The 0.5 eV contour in the $O + H_2$ arrangement channel region spreads over that entire region for the LEPS PES, whereas for the RMOS and GLDP PESs that contour is closed. The GLDP contours display small wiggles near the central region of the plot. This is the region for which the ab initio geometries were selected from both OHH and HOH configurations. Small differences in the ab initio data for these configurations can cause such features. The RMOS fit imposed a cubic spline smoothing in this region and as a result does not display this behavior. The GLDP surface is hatched for energies below 2 eV, to show the most accessible regions of the surface for reaction energies below that value. Figure 4d shows the difference between the RMOS and GLDP surface for the GLDP abstraction saddle-point hyperradius. The hatching covers the regions for which these differences are less than 0.5 kcal/mol (~0.02 eV) in absolute value. This region significantly overlaps the area below 2 eV of panel 4b. This suggests that cross sections for the abstraction reaction on the $^3A''$ GLDP and

Figure 4. Equipotential contours on equatorial views of the $^3A''$ surface for selected hyperradii ρ. (a) LEPS surface at its $\rho = 4.3427$ b abstraction saddle point. (b) High-accuracy GLDP surface at its $\rho = 4.5047$ b abstraction saddle point. The hatched regions correspond to energies below 2 eV. (c) RMOS surface at its $\rho = 4.5100$ b abstraction saddle point. (d) Differences between RMOS and GLDP energies at ρ 4.5047 b. The hatched regions correspond to configurations for which the agreement between these surfaces is better than 0.5 kcal/mol. (e) Correction surface at $\rho = 4.5047$ b. (f) Correction surface at $\rho = 3.2849$ b. (g) LEPS surface at its $\rho = 3.0375$ b exchange saddle point. (h) High-accuracy GLDP surface at its $\rho = 3.2849$ b exchange saddle point. The hatched regions correspond to energies below 2 eV. (i) RMOS surface at its $\rho = 3.2710$ b exchange saddle point. (j) Differences between RMOS and GLDP energies at $\rho = 3.2849$ b. The hatched regions correspond to configurations for which the agreement between these surfaces is better than 0.5 kcal/mol. The numbers associated with the contours indicate the energy values along them, and their energy spacing is 0.5 eV for panels a−c and g−i, 0.5 kcal/mol for panels d and j, and 0.1 kcal/mol for panels e and f. The position of the saddle points is indicated by + in panels a−e and × in panels f−j. The radius of the circle that surrounds each panel is $\rho(\pi/2)$, and this value defines the corresponding distance scale.

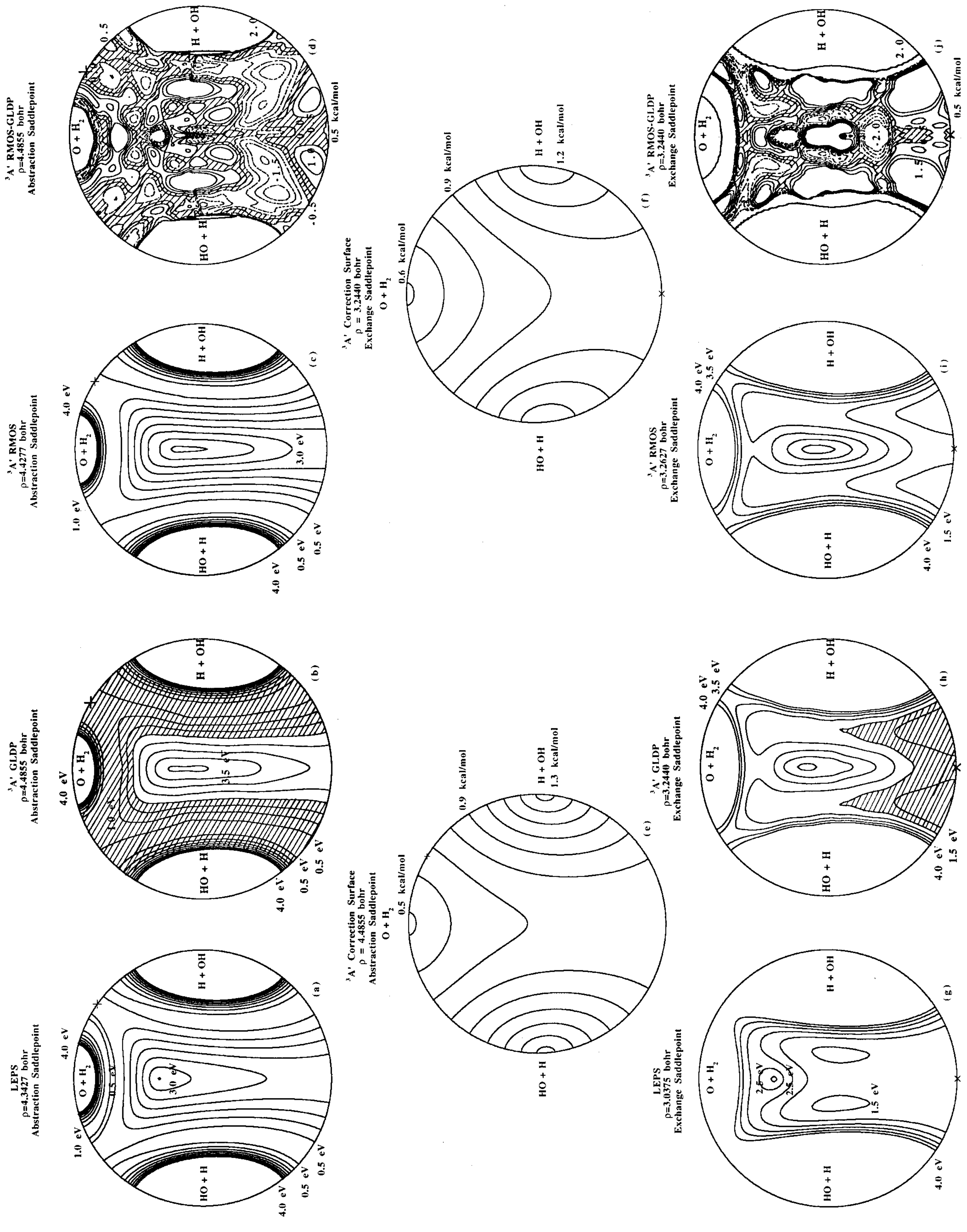
LEPS
ρ=4.3427 bohr
Abstraction Saddlepoint
O + H$_2$
HO + H
H + OH
1.0 eV
4.0 eV
0.5 eV
3.0 eV
4.0 eV
0.5 eV
0.5 eV
(a)
^{3}A' GLDP
ρ=4.4855 bohr
Abstraction Saddlepoint
O + H$_2$
HO + H
H + OH
4.0 eV
1.0 eV
3.5 eV
4.0 eV
0.5 eV
0.5 eV
(b)
^{3}A' RMOS
ρ=4.4277 bohr
Abstraction Saddlepoint
O + H$_2$
HO + H
H + OH
1.0 eV
4.0 eV
3.0 eV
4.0 eV
0.5 eV
0.5 eV
(c)
^{3}A' RMOS-GLDP
ρ=4.4855 bohr
Abstraction Saddlepoint
O + H$_2$
HO + H
H + OH
0.5
2.0
-0.5
1.0
0.5 kcal/mol
(d)
^{3}A' Correction Surface
ρ = 4.4855 bohr
Abstraction Saddlepoint
O + H$_2$
0.5 kcal/mol
0.9 kcal/mol
H + OH
1.3 kcal/mol
HO + H
(e)
^{3}A' Correction Surface
ρ = 3.2440 bohr
Exchange Saddlepoint
O + H$_2$
0.6 kcal/mol
0.9 kcal/mol
H + OH
1.2 kcal/mol
HO + H
(f)
LEPS
ρ=3.0375 bohr
Exchange Saddlepoint
O + H$_2$
HO + H
H + OH
2.5 eV
2.5 eV
1.5 eV
4.0 eV
(g)
^{3}A' GLDP
ρ=3.2440 bohr
Exchange Saddlepoint
O + H$_2$
HO + H
H + OH
4.0 eV
3.5 eV
4.0 eV
1.5 eV
(h)
^{3}A' RMOS
ρ=3.2627 bohr
Exchange Saddlepoint
O + H$_2$
HO + H
H + OH
4.0 eV
3.5 eV
4.0 eV
1.5 eV
(i)
^{3}A' RMOS-GLDP
ρ=3.2440 bohr
Exchange Saddlepoint
O + H$_2$
HO + H
H + OH
2.0
2.0
1.5
0.5 kcal/mol
(j)

Figure 5. Equipotential contours on equatorial views of the $^3A'$ surface for selected hyperradii ρ. (a) LEPS surface at its $\rho = 4.3427$ b abstraction saddle point. (b) High-accuracy GLDP surface at its $\rho = 4.4855$ b abstraction saddle point. The hatched regions correspond to energies below 2 eV. (c) RMOS surface at its $\rho = 4.4277$ b abstraction saddlepoint. (d) Differences between RMOS and GLDP energies at ρ 4.4855 b. The hatched regions correspond to configurations for which the agreement between these surfaces is better than 0.5 kcal/mol. (e) Correction surface at $\rho = 4.4855$ b. (f) Correction surface at $\rho = 3.2440$ b. (g) LEPS surface at its $\rho = 3.0375$ b exchange saddle point. (h) High-accuracy GLDP surface at its $\rho = 3.2440$ b exchange saddle point. The hatched regions correspond to energies below 2 eV. (i) RMOS surface at its $\rho = 3.2627$ b exchange saddle point. (j) Differences between RMOS and GLDP energies at $\rho = 3.2440$ b. The hatched regions correspond to configurations for which the agreement between these surfaces is better than 0.5 kcal/mol. The numbers associated with the contours indicate the energy values along them, and their energy spacing is 0.5 eV for panels a−c and g−i, 0.5 kcal/mol for panels d and j and 0.1 kcal/mol for panels e and f. The position of the saddle points is indicated by + in panels a−e and × in panels f−j. The radius of the circle that surrounds each panel is $\rho(\pi/2)$, and this value defines the corresponding distance scale.

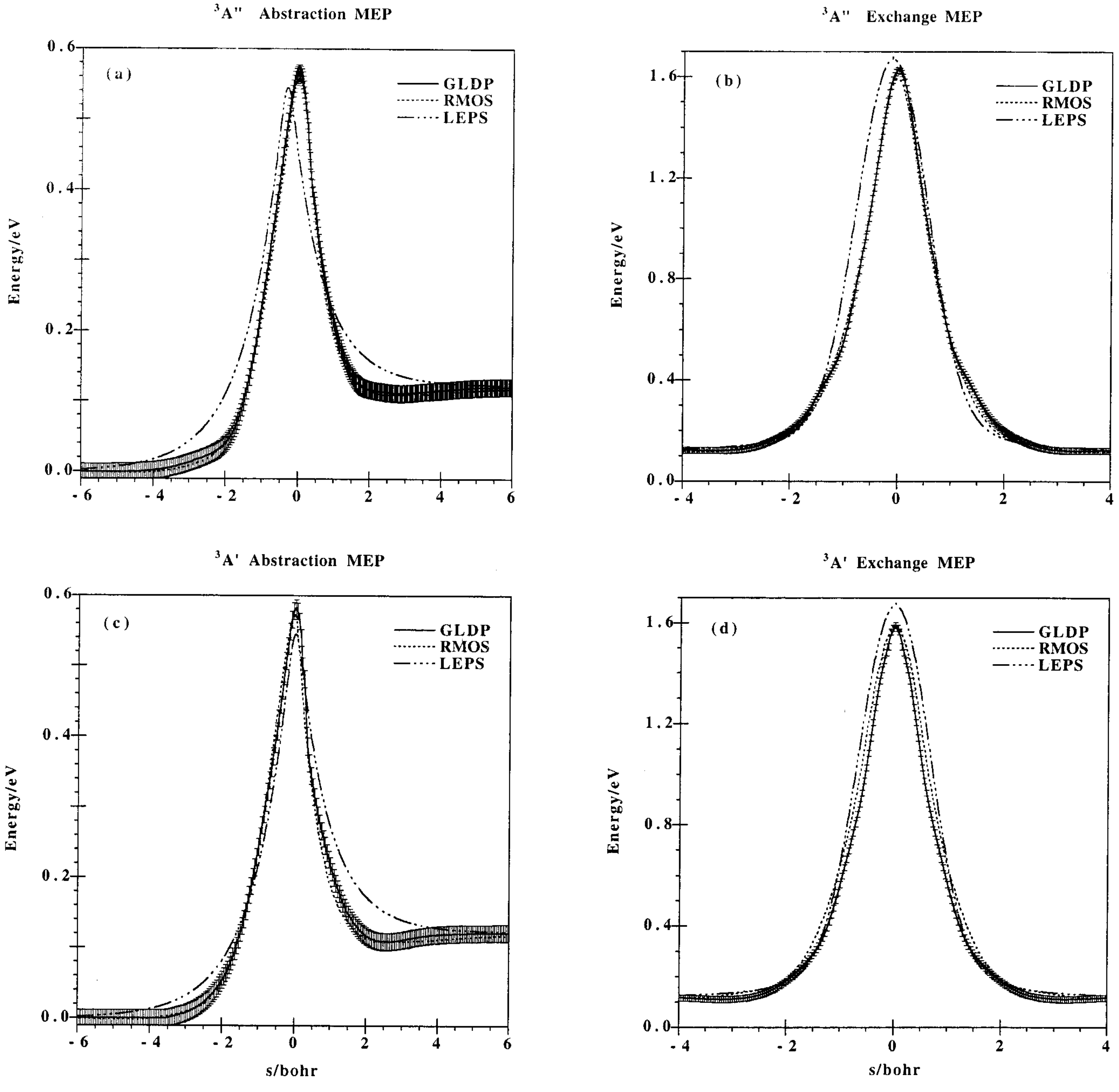

Figure 6. Minimum-energy path energies, calculated in mass-scaled coordinates, for the GLDP (solid curves), RMOS (dotted curves), and LEPS (dash−dotted curves) surfaces, as a function of the distance s along the minimum-energy path. The values s_0 of s for the three PESs are set equal to each other at a large value of the Jacobi mass-scaled coordinate R_O or R_H, chosen so that the peak in the GLDP MEP occurs at $s = 0$. (a) $^3A''$ abstraction MEP, $s_0 = -6.0$ b, $R_O = 10.322$ b. (b) $^3A''$ exchange MEP, $s_0 = -4.0$ b, $R_O = 6.2598$ b. (c) $^3A'$ abstraction MEP, $s_0 = -6.0$ b, $R_O = 10.258$ b. (d) $^3A'$ exchange MEP, $s_0 = -4.0$ b, $R_O = 6.2478$ b. Error bars on the GLDP paths show the rms error of the surfaces, 0.27 kcal/mol for $^3A''$ and 0.28 kcal/mol for $^3A'$. The small horizontal lines indicate the top and bottom of these error bars.

RMOS high-accuracy PESs might be close to each other. Regions near the saddle point are in very good agreement. Regions near the H + OH exchange pathway display larger differences, up to 1.5 kcal/mol.

Panels g−j correspond to the exchange saddle points ρ. There are significant differences between the LEPS surface and the GLDP and RMOS ones for the $O + H_2$ arrangement channel region. At this hyperradius the LEPS PES has a small barrier

TABLE 9: Surface Fitting Errors

error (kcal/mol)	$^3A''$			$^3A'$		
	GLDP reg.	GLDP high	RMOS high	GLDP reg.	GLDP high	RMOS high
rms	0.27	0.27	0.42	0.28	0.28	0.53
max[a]	0.39	0.39	2.38	0.38	0.38	2.44

[a] Maximum absolute value error.

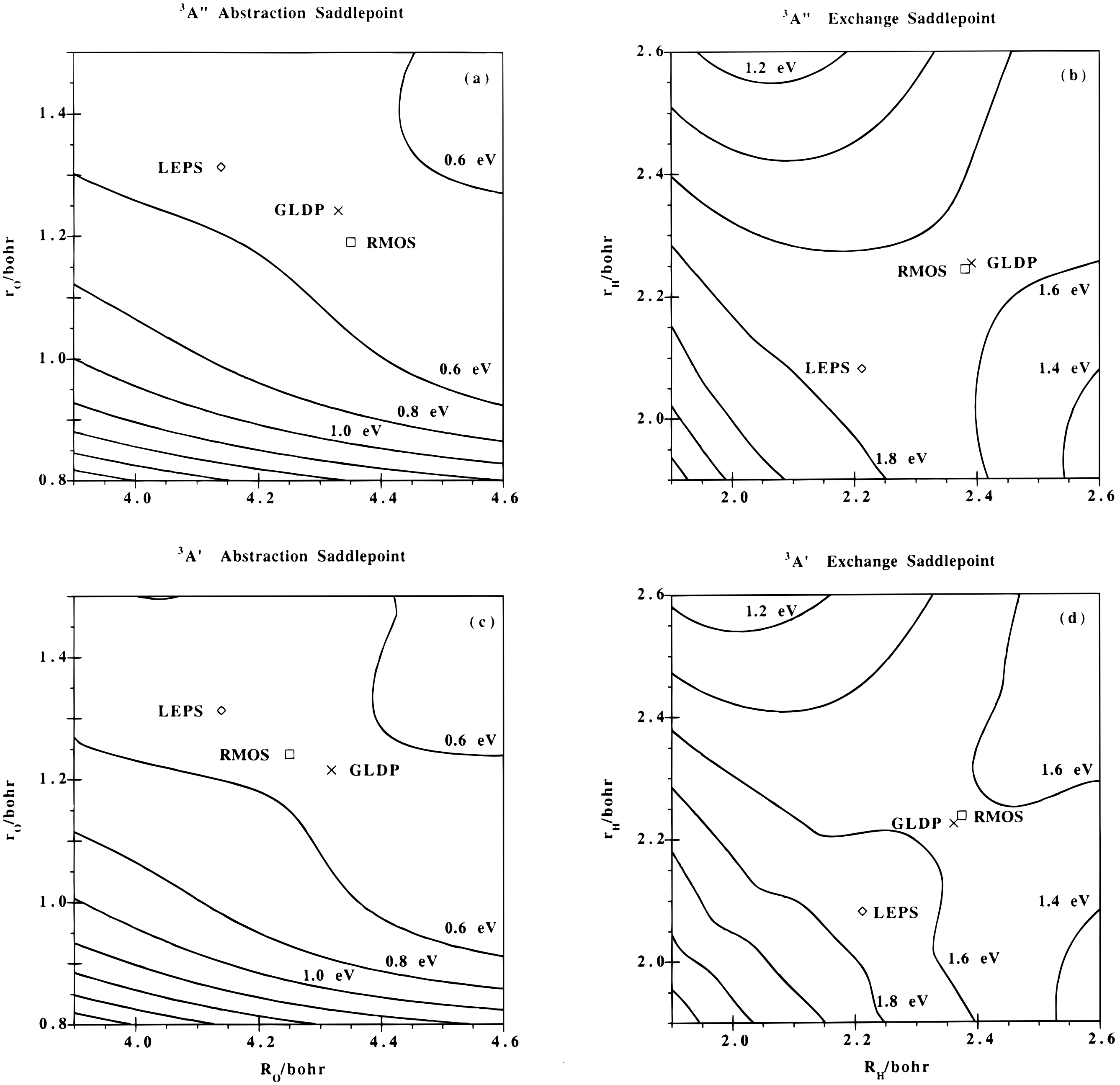

Figure 7. Comparison of saddle-point geometries. The GLDP, RMOS, and LEPS saddle points and mass-scaled collinear equipotential contours of the high-accuracy GLDP surface are depicted for (a) the $^3A''$ abstraction collinear configuration (H being the middle atom), (b) the $^3A''$ exchange collinear configuration (O being the middle atom), (c) the $^3A'$ abstraction collinear configuration, and (d) the $^3A'$ exchange collinear configuration.

Figure 8. Mass-scaled collinear equipotential contours for GLDP surface. (a) Equipotential contours (solid curves) and MEP (dotted curve) for the collinear $^3A''$ GLDP abstraction (H in the middle) configuration. (b) Contours of the differences between the $^3A''$ RMOS and GLDP PESs. (c) Contours of the differences between the LEPS and $^3A''$ GLDP abstraction collinear configurations. Similar plots are presented for the $^3A''$ exchange (O in the middle) configurations (panels d−f), the $^3A'$ abstraction configurations (panels g−i), and the $^3A'$ exchange configurations (panels j−l). The saddle points are denoted by +. The hatched regions in panels a, d, g, and j correspond to energies below 2.0 eV. The remaining hatched regions indicate agreement to within 0.5 kcal/mol.

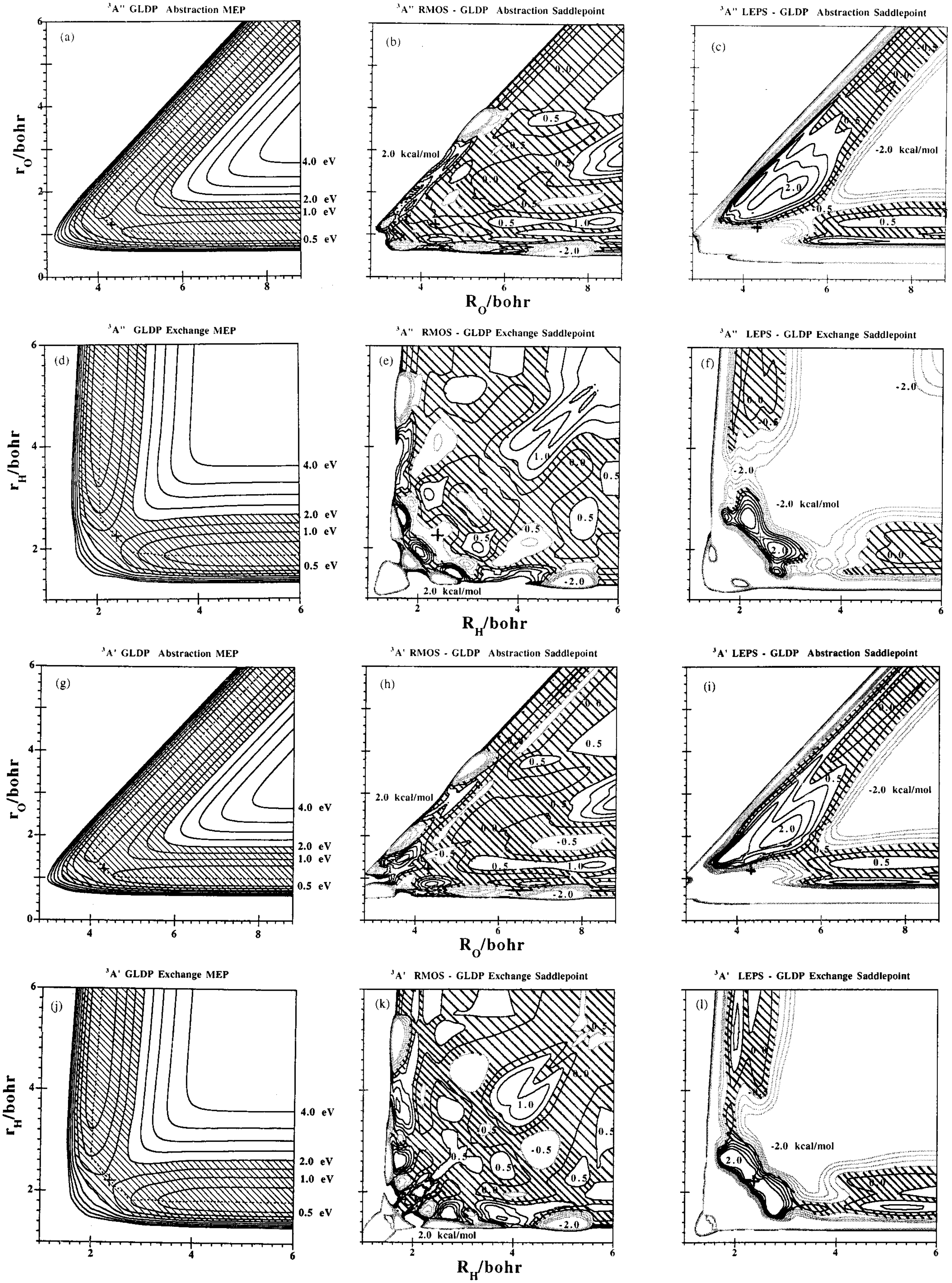
³A" GLDP Abstraction MEP
³A" RMOS - GLDP Abstraction Saddlepoint
³A" LEPS - GLDP Abstraction Saddlepoint
(a)
(b)
(c)
r_O/bohr
4.0 eV
2.0 eV
1.0 eV
0.5 eV
2.0 kcal/mol
-2.0 kcal/mol
R_O/bohr
³A" GLDP Exchange MEP
³A" RMOS - GLDP Exchange Saddlepoint
³A" LEPS - GLDP Exchange Saddlepoint
(d)
(e)
(f)
r_H/bohr
R_H/bohr
³A' GLDP Abstraction MEP
³A' RMOS - GLDP Abstraction Saddlepoint
³A' LEPS - GLDP Abstraction Saddlepoint
(g)
(h)
(i)
³A' GLDP Exchange MEP
³A' RMOS - GLDP Exchange Saddlepoint
³A' LEPS - GLDP Exchange Saddlepoint
(j)
(k)
(l)

TABLE 10: Abstraction Saddle-Point Properties[a]

	$^3A''$			$^3A'$	
	GLDP	RMOS	LEPS	GLDP	RMOS
R'_{OH} (b)	2.3004	2.3502	2.113	2.3096	2.2425
R'_{HH} (b)	1.7058	1.6352	1.801	1.7050	1.6693
E (kcal/mol)	13.04	13.26	12.49	13.22	13.44
E (eV)	0.565	0.575	0.542	0.573	0.583

[a] The R'_{OH} and R'_{HH} represent non-mass-scaled internuclear distances.

TABLE 11: Exchange Saddle-Point Properties[a]

	$^3A''$			$^3A'$	
	GLDP	RMOS	LEPS	GLDP	RMOS
$R'_{OH} = R'_{OH'}$ (b)	2.2554	2.2458	2.103	2.2402	2.2273
E (kcal/mol)	44.41	36.83	38.5	36.80	36.67
E (eV)	1.626	1.597	1.67	1.596	1.590

[a] The R'_{OH} and $R'_{OH'}$ represent non-mass-scaled internuclear distances.

in this region which is not present in either of the other two. In this O + H_2 region, the LEPS PES has significantly higher energies than the GLDP and RMOS ones. Overall, the LEPS energies at the exchange saddle point ρ are higher than either the GLDP or RMOS ones. In panel h, corresponding to the GLDP surface, the regions for which the energy is below 2 eV is indicated by the hatching. Again the GLDP surface shows wiggles in the equipotential contours in the switch-over region from OHH to HOH geometries. The hatched regions of panel j indicate agreement between the RMOS and GLDP energies to within 0.5 kcal/mol. There are slightly larger differences between the RMOS and GLDP energies for the exchange ρ than for the abstraction one.

The same plots are shown for the $^3A'$ surfaces in Figure 5. The LEPS panels are the same as for Figure 4, but repeated here for easy comparison. The GLDP and RMOS $^3A'$ surfaces have higher energies than their $^3A''$ counterparts. The abstraction saddle-point hypersphere has regions in its center with energies above 4 eV. The $^3A''$ surfaces did not reach 3.5 eV in this region. There is no 0.5 eV contour in the O + H_2 arrangement channel region. Differences between the RMOS and GLDP $^3A'$ surfaces are larger than in the $^3A''$ case, as depicted by the smaller size of the hatched area of agreement to within 0.5 kcal/mol. The exchange saddle point ρ contours again show large differences between the LEPS and the GLDP and RMOS energies. Most of the hatched region below 2 eV in the GLDP panel corresponds to geometries whose energies differ from the RMOS energies by more than 0.5 kcal/mol in absolute value. A very small portion of the difference plot, panel j, corresponds to an agreement between those two fits to within 0.5 kcal/mol, suggesting that they could display significant dynamics differences.

A comparison of the energy along the MEPs is presented in Figure 6. In panel a, the energy for the MEP of the $^3A''$ abstraction path is plotted against the distances along that path, and the error bars represent the rms fitting error of that surface. The origin $s = 0$ is chosen to correspond to the peak of the GLDP MEP. For $s = -6.0$ b, the value of R_O for this PES is 10.322 b, which represents a point in the asymptotic O + H_2 region. The three MEPs start at this R_O with the same value of s. This allows one to view differences in the position of the saddle points among the surfaces. Figure 7 shows the positions of the three surfaces saddle points and equipotential contours of the collinear GLDP surfaces. Panel (a) depicts the positions of the LEPS, GLDP, and RMOS $^3A''$ abstraction saddle points and contours of the collinear abstraction GLDP PES. The RMOS saddle point occurs earliest (i.e., at the largest R_O) in the reaction path, followed closely by the GLDP saddle point, with the LEPS saddle point being last and further removed from and lower than the other two. The GLDP and RMOS surfaces have very similar MEP potentials, with only minor differences near the top and at the bottom of the barriers. The LEPS MEP potential has a wider barrier that peaks 0.5 kcal/mol lower than the GLDP barrier. The GLDP and RMOS MEP potentials have a broad well of depth 0.2 kcal/mol for $s > 0$, which is present in the ab initio data and is not an artifact of the fitting. All minimum energy paths are along collinear configurations. Table 10 gives the position and height of the abstraction saddle point for the various surfaces. The GLDP abstraction barrier has a height of 13.04 kcal/mol, and the RMOS one is 13.26 kcal/mol. The difference between the two is within the rms error of either surface. The LEPS barrier is 12.49 kcal/mol,[6,10] smaller than either of the other two.

The energy along the exchange MEP is given in Figure 6b. The curves all start from $s = -4.0$ b and a Jacobi mass-scaled R_H value of 6.2598 b in the OH asymptotic region. Again, the GLDP and RMOS barriers are similar, and the LEPS one is wider. However, the LEPS barrier is now higher than the other two. The exchange saddle point properties are given in Table 11. The GLDP barrier height is 1.626 eV. The RMOS barrier height of 1.597 eV is slightly smaller. The LEPS barrier, which was corrected from its original low value by Schatz,[6] is 1.67 eV. The relative position of the saddle points can be seen in Figure 7b. The RMOS and GLDP exchange saddle points are very close, and the LEPS saddlepoint is 0.2 b shorter in the mass-scaled Jacobi R_H.

The $^3A'$ minimum-energy paths are given in Figure 6c,d. The two surfaces, $^3A'$ and $^3A''$, are degenerate for collinear configurations. This property is displayed by the ab initio data. However, the fitting methods used are global methods and as such may produce small differences in the collinear configuration energies. The GLDP abstraction path has a well after the barrier along the exit channel that is 0.1 kcal/mol deeper than the $^3A''$ GLDP well. These minor differences are however less than the rms error of the surfaces. The distance along the paths in Figure 6(c) are set equal to -6.0 b for a Jacobi mass-scaled $R_O = 10.258$ b. The saddle-point positions are compared in Figure 7c. The RMOS and GLDP abstraction saddle points are close to each other, with the order switched from the $^3A''$ ordering. The LEPS saddle point is closer to them than it was for the $^3A''$ abstraction saddle point. As shown in Table 10, the $^3A'$ barrier heights are 0.2 kcal/mol higher than the corresponding $^3A''$ ones. This is another consequence of the fitting error. The exchange $^3A'$ MEP barrier of Figure 6d agrees better with the LEPS one than did the $^3A''$ barrier, the LEPS being however wider as was also the case when compared to the $^3A''$ one. The distance along the MEPs are set equal to -4.0 b at $R_H = 6.2478$ b for the three curves, and the barriers are better aligned than for the $^3A''$ surface. The saddle-point positions are switched as in the abstraction case. Figure 7d shows that the RMOS and GLDP saddle points are close to each other, with the RMOS one occurring at a slightly larger R_H. The LEPS saddle point is located at a R_H that is 0.2 b smaller. The $^3A'$ barrier heights, as shown in Table 11, are smaller than the corresponding $^3A''$ ones.

Figure 8 displays equipotential contours for the high-accuracy GLDP surface in mass-scaled Jacobi coordinates, along with contours of the differences between the RMOS and LEPS energies. The $^3A''$ abstraction collinear configurations are displayed in panels (a−c). It is obvious that more of the accessible regions for reaction are in agreement with the RMOS

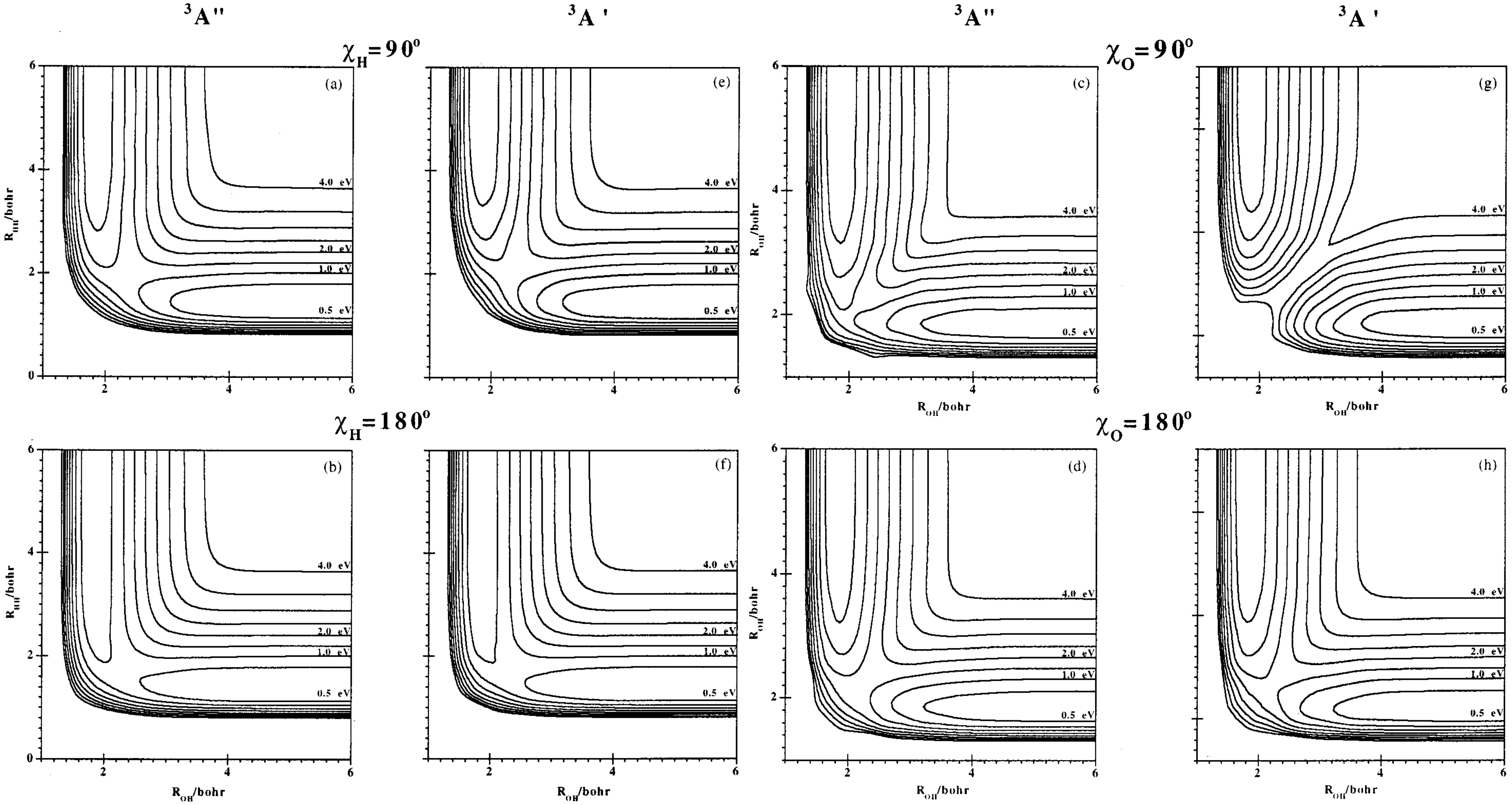

Figure 9. Comparison of the $^3A''$ and $^3A'$ GLDP PESs at different bond angles. Equipotential contours of the $^3A''$ GLDP high-accuracy surface (panels a−d) and the $^3A'$ GLDP high-accuracy surface (panels e−h) are given for fixed bond angles χ_H and χ_O of 90° and 180°.

than with the LEPS surface. Contours for the $^3A''$ exchange collinear configuration are depicted in panels (d−f). Again the RMOS surface agrees with the GLDP one to a greater extent than does the LEPS PES, and nearly all of the regions below 2 eV of the first two differ by less than 0.5 kcal/mol. The $^3A'$ surfaces, for the abstraction collinear configuration (Figure 8g−i) and the exchange collinear configuration (Figure 8j−l), are nearly identical to those for the $^3A''$ surfaces, suggesting that the two fitting methods used yield similar differences between the $^3A''$ and $^3A'$ surfaces.

Figure 9 displays contours for the GLDP surface for fixed values of the bond angles χ_H and χ_O equal to 180° and 90°. For the constant χ_H plots, panels a and b for $^3A''$ and e and f for $^3A'$, show no noticeable differences for a given χ_H. The $\chi_O = 90°$ contours, given in panels c and g, show major differences. The $^3A'$ PES has a barrier to reaction in excess of 3.5 eV at this angle, whereas the $^3A''$ barrier is slightly larger than 1.5 eV, nearly a 2 eV difference. The $\chi_O = 180°$ plots d and h are again similar. This is another degenerate collinear configuration for the $^3A''$ and $^3A'$ states. The contours displayed in Figure 9 do not sample the crossover region from OHH configurations to HOH configurations, and as a result the wiggles apparent in Figures 4 and 5 for the GLDP PES are now absent.

Overall, the GLDP fit and RMOS fit to the ab initio data are very similar. The GLDP has a higher fitting accuracy although the RMOS displays a more physical behavior. There were no unphysical features that had to be removed from the RMOS surface, whereas in the GLDP fit many unphysical wells had to be eliminated.

4. Summary

We have calculated and fitted potential energy surfaces for the lowest $^3A'$ and lowest $^3A''$ electronic states of OH_2. These PESs have chemical accuracy (about 0.3 kcal/mol), are devoid of apparent unphysical features, and should yield accurate cross sections when used in accurate quantum reactive scattering calculations. The determination of these PESs benefited by an iterative approach between ab initio calculations and surface fittings. By fitting an initial set of data, followed by further ab initio calculations for additional geometries, and refitting, we were able to achieve a better fitting accuracy with fewer data than would otherwise be possible. The elimination of unphysical features caused by the form of the fitting function was accomplished by the introduction of virtual points and localized Gaussians. These are invaluable fitting tools. A full listing of the regular-accuracy ab initio data, the 112 high-accuracy ab initio data, and their fits and the final GLDP $^3A'$ and $^3A''$ fitted surfaces are available upon request.

We have generated chemically accurate potential energy surfaces using less computer resources than might otherwise be necessary by performing high-accuracy ab initio calculations on about 12% of the set of geometries for which regular accuracy calculations were done and fitting the differences between these calculations. This correction surface was used to raise the regular-accuracy calculations to the high-accuracy level. The two resulting surfaces, one for $^3A'$ and one for $^3A''$, are the best currently available.

It will be interesting to determine in future accurate scattering calculations whether or not the different fitting methods used result in different reaction cross sections.

References and Notes

(1) Dixon-Lewis, G.; Williams, D. J. *Comput. Chem. Kinet.* **1977**, *17*, 1.

(2) Howard, R. E.; McLean, A. D.; Lester, W. A., Jr. *J. Chem. Phys.* **1979**, *71*, 2412.

(3) Light, G. C. *J. Chem. Phys.* **1978**, *68*, 2831.

(4) Westburg, K.; Cohen, N. *J. Chem. Phys. Ref. Data* **1983**, *12*, 531.

(5) Presser, N.; Gordon, R. J. *J. Chem. Phys.* **1985**, *82*, 1291.

(6) Schatz, G. C. *J. Chem. Phys.* **1985**, *83*, 5677.

(7) Koppe, S.; Laurent, T.; Naik, P. D.; Volpp, H.-R.; Wolfrum, J.; Arusi-Parpar, T.; Bar, I.; Rosenwaks, S. *Chem. Phys. Lett.* **1993**, *214*, 546.

(8) Chatfield, D. C.; Friedman, R. S.; Lynch, G. C.; Truhlar, D. G.; Schwenke, D. W. *J. Chem. Phys.* **1993**, *98*, 342.

(9) Whitlock, P. A.; Muckerman, J. T.; Fisher, E. P. In *Theoretical Investigations of the Reaction of O(^{3}P,^{1}D) and C(^{1}D) + H$_2$*; Research Institute for Engineering Sciences, Wayne State University: Detroit, MI, 1976.

(10) Johnson, B. R.; Winter, N. W. *J. Chem. Phys.* **1977**, *66*, 4116.

(11) Clary, D. C.; Connor, J. N. L.; Edge, C. J. *Chem. Phys. Lett.* **1979**, *68*, 154.

(12) Schinke, R.; Lester, W. A. *J. Chem. Phys.* **1979**, *70*, 4893.

(13) Broida, M.; Persky, A. *J. Chem. Phys.* **1984**, *80*, 3687.

(14) Westenberg, A. H.; Haas, N. *J. Chem. Phys.* **1967**, *47*, 4242.

(15) Mayer, S. W.; Schieler, L. *J. Chem. Phys.* **1968**, *72*, 2628.

(16) Garrett, B. C.; Truhlar, D. G.; Grev, R. S.; Magnuson, A. W. *J. Phys. Chem.* **1980**, *84*, 1730.

(17) Walch, S. P.; Wagner, A. F.; Dunning, T. H.; Schatz, G. C. *J. Chem. Phys.* **1980**, *72*, 2894.

(18) Schatz, G. C.; Wagner, A. F.; Walch, S. P.; Bowman, J. M. *J. Chem. Phys.* **1981**, *74*, 4984.

(19) Garrett, B. C.; Truhlar, D. G.; Bowman, J. M.; Wagner, A. F.; Robie, D.; Arepalli, S.; Presser, N.; Gordon, R. J. *J. Am. Chem. Soc.* **1986**, *108*, 3515.

(20) Garrett, B. C.; Truhlar, D. G *Int. J. Quantum Chem.* **1987**, *31*, 17.

(21) Bowman, J. M.; Wagner, A. F.; Walch, S. P.; Dunning, T. H. *J. Chem. Phys.* **1984**, *81*, 1739.

(22) Garrett, B. C.; Truhlar, D. G.; Schatz, G. C. *J. Am. Chem. Soc.* **1986**, *108*, 2876.

(23) Lynch, G. C.; Halvick, P.; Truhlar, D. G.; Garrett, B. C.; Schwenke, D. W.; Kouri, D. J. *Z. fur Naturforsch.* **1989**, *44a*, 427.

(24) Halvick, P.; Zhao, M.; Truhlar, D. G.; Schwenke, D. W.; Kouri, D. J. *J. Chem. Soc., Faraday Trans.* **1990**, *86*, 1705.

(25) Garrett, B. C.; Truhlar, D. G. *J. Am. Chem. Soc.* **1979**, *83*, 1915.

(26) Walch, S. P.; Dunning, T. H.; Bobrowicz, F. W.; Raffenetti, R. *J. Chem. Phys.* **1980**, *72*, 406.

(27) Garrett, B. C.; Truhlar, D. G. *Int. J. Quantum Chem.* **1986**, *29*, 1463.

(28) Joseph, T.; Truhlar, D. G.; Garrett, B. C. *J. Chem. Phys.* **1988**, *88*, 6982.

(29) Lee, K. T.; Bowman, J. M.; Wagner, A. F.; Schatz, G. *J. Chem. Phys.* **1982**, *76*, 3583.

(30) Truhlar, D. G.; Runge, K.; Garrett, B. C. *Proceedings of the 20th International Symposium of Combustion*; The Combustion Institute: Pittsburgh, PA, 1984; p 585.

(31) Lee, K. T.; Bowman, J. M.; Wagner, A. F.; Schatz, G. *J. Chem. Phys.* **1982**, *76*, 3563.

(32) Knowles, P.; Werner, H.-J. *Chem. Phys. Lett.* **1988**, *145*, 514.

(33) Werner, H.; Knowles, P. *J. Chem. Phys.* **1988**, *89*, 5803.

(34) Dunning, T., Jr. *J. Chem. Phys.* **1989**, *90*, 1007.

(35) Kuntz, P. J.; Roach, A. C. *J. Chem. Soc., Faraday Trans. 2* **1972**, *68*, 259.

(36) Bowman, J. M.; Kuppermann, A. *Chem. Phys. Lett.* **1975**, *34*, 523.

(37) Connor, J. N. L.; Jakubetz, W.; Manz, J. *Mol. Phys.* **1975**, *29*, 347.

(38) Gray, S. K.; Wright, J. S. *J. Chem. Phys.* **1977**, *66*, 2867.

(39) Wright, J. S.; Gray, S. K. *J. Chem. Phys.* **1978**, *69*, 67.

(40) Mayne, H. R.; Polanyi, J. C.; Sathyamurthy, N.; Raynor, S. *J. Chem. Phys.* **1984**, *88*, 4064.

(41) Wright, J. S.; Kruus, E. *J. Chem. Phys.* **1986**, *85*, 7251.

(42) Schatz, G. C. *Rev. Mod. Phys.* **1989**, *61*, 669.

(43) Peng, Z.; Kuppermann, A. *Chem. Phys. Lett.* **1990**, *175*, 242. Peng, Z.; Kristyan, S.; Kuppermann, A.; Wright, J. S. *Phys. Rev. A* **1995**, *52*, 1005.

(44) Skokov, S.; Peterson, K. A.; Bowman, J. M. *J. Chem. Phys.* **1998**, *123*, 4567.

(45) Ho, T.; Rabitz, H. *J. Chem. Phys.* **1996**, *104*, 2584.

(46) Schatz, G. C.; Papaioannou, A.; Pederson, L.; Harding, L. B.; Hollebeek, T.; Ho, T.-S.; Rabitz, H. *J. Chem. Phys.* **1997**, *107*, 2340.

(47) Jordan, M. J. T.; Thompson, K. C.; Collins, M. A. *J. Chem. Phys.* **1995**, *102*, 5647.

(48) Frishman, A.; Hoffman, D. K.; Kouri, D. J. *J. Chem. Phys.* **1997**, *107*, 804.

(49) Garcia, E.; Laganá, A. *Mol. Phys.* **1984**, *52*, 1115.

(50) Murrell, J. N.; Carter, S.; Farantos, S.; Huxley, P.; Varandas, A. J. C. *Molecular Potential Energy Functions*; Wiley: Chichester, 1984.

(51) Aguado, A.; Paniagua, M. *J. Chem. Phys.* **1992**, *96*, 1265.

(52) Aguado, A.; Súarez, C.; Paniagua, M. *J. Chem. Phys.* **1994**, *101*, 4004.

(53) Parker, G. A.; Laganá, A.; Crocchianti, S.; Pack, R. T. *J. Chem. Phys.* **1995**, *102*, 1238.

(54) Wu, Y.-S. M.; Cuccaro, S. A.; Hipes, P. G.; Kuppermann, A. *Chem. Phys. Lett.* **1990**, *168*, 429.

(55) Wu, Y.-S. M.; Cuccaro, S. A.; Hipes, P. G.; Kuppermann, A. *Theor. Chim. Acta* **1991**, *79*, 225.

(56) Wu, Y.-S. M.; Kuppermann, A.; Lepetit, B. *Chem. Phys. Lett.* **1991**, *186*, 319.

(57) Feller, D. F.; Ruedenberg, K. *Theor. Chim. Acta* **1979**, *52*, 231.

(58) Langhoff, S.; Davidson, E. R. *Int. J. Quantum Chem.* **1974**, *8*, 61.

(59) Schatz, G. C. In *Potential Energy Surfaces and Dynamics Calculations*; Truhlar, D. G., Ed.; Plenum: New York, 1981; p 287.

(60) Garrett, B. C.; Truhlar, D. G.; Wagner, A. F.; Dunning, T. H. *J. Chem. Phys.* **1983**, *78*, 4400.

(61) Wright, J. S.; Donaldson, D. J.; Williams, R. J. *J. Chem. Phys.* **1984**, *81*, 397.

(62) Joseph, T.; Truhlar, D. G.; Garrett, B. C. *J. Chem. Phys.* **1988**, *88*, 6982.

(63) Hamming, R. W. *Numerical Methods for Scientists and Engineers*, 2nd ed.; McGraw-Hill: New York, 1973; pp 349−356.

(64) Marquardt, D. W. *J. Soc. Ind. Appl. Math.* **1963**, *11*, 431.

(65) Press, W. H.; Flannery, B. H.; Tenkolsky, S. A.; Vetterling, W. T. *Numerical Recipes (Fortran)*; Cambridge University Press: Cambridge, 1986; pp 523−528.

(66) Hamilton, I. P.; Light, J. C.; Whaley, K. B. *J. Chem. Phys.* **1986**, *85*, 5151.

(67) London, F. *Z. Electrochem.* **1929**, *35*, 1722.

(68) Eyring, H.; Polanyi, M. *Z. Phys. Chem.* **1931**, *12*, 279.

(69) Sato, S. *J. Chem. Phys.* **1955**, *23*, 592.

(70) Sato, S. *J. Chem. Phys.* **1955**, *23*, 2465.

(71) Kuntz, P. J.; Nemeth, E. M.; Planyi, J. C.; Rosner, S. D.; Young, C. E. *J. Chem. Phys.* **1966**, *44*, 1168.

(72) Hu, W. P.; Liu, Y. P.; Truhlar, D. G. *J. Chem. Soc., Faraday Trans.* **1994**, *90*, 1715.

(73) Quapp, W.; Heidrich, D. *Theor. Chim. Acta* **1984**, *66*, 245.

(74) Fukui, K. *J. Phys. Chem.* **1970**, *74*, 4161.

(75) Tachibana, A.; Fukui, K. *Theor. Chim. Acta* **1978**, *49*, 321.

(76) Martin, J. M. L. *Chem. Phys. Lett.* **1996**, *259*, 669.

(77) Peterson, K.; Dunning, T., Jr. *J. Phys. Chem.* **1997**, *101*, 6280.

(78) Walch, S. *J. Chem. Phys.* **1987**, *86*, 5670.

(79) Kendall, R.; Dunning, T. H., Jr.; Harrison, R. *J. Chem. Phys.* **1992**, *96*, 6796.

(80) Woon, D.; Dunning, T., Jr. *J. Chem. Phys.* **1993**, *99*, 1914.

(81) Schatz, G. C. *J. Phys. Chem.* **1995**, *99*, 7522.

(82) Schatz, G. C.; McCabe, P.; Connor, J. N. L. *Faraday Discuss.* **1998**, *110*, 139.

(83) Maierle, C. S.; Schatz, G. C.; Gordon, M. S.; McCabe, P.; Connor, J. N. L. *J. Chem. Soc., Faraday Trans.* **1997**, *93*, 709.

(84) Alexander, M. H.; Werner, H.-J.; Manolopoulos, D. E. *J. Chem. Phys.* **1998**, *109*, 5710.

(85) Stark, K.; Werner, H.-J. *J. Chem. Phys.* **1996**, *104*, 6515.

(86) Castillo, J. F.; Manolopoulos, D. E.; Stark, K.; Werner, H.-J. *J. Chem. Phys.* **1996**, *104*, 6531.

(87) Moore, C. E. Atomic Energy Levels *Natl. Bur. Stand. (U.S.) Circ.* **1949**, *I* (467), 45.

(88) Delves, L. M. *Nucl. Phys.* **1959**, *9*, 391.

(89) Delves, L. M. *Nucl. Phys.* **1960**, *20*, 275.

(90) Jepsen, D.; Hirschfelder, J. O. *Proc. Natl. Acad. Sci. U.S.A.* **1959**, *45*, 249.

(91) Smith, F. T. *J. Math. Phys.* **1962**, *3*, 735.

(92) Kuppermann, A. *Chem. Phys. Lett.* **1975**, *32*, 374.

(93) Kuppermann, A. In *Advances in Molecular Vibrations and Collision Dynamics*; JAI Press: Greenwich, CT, 1993; Vol. 2B, pp 117−186.